JOURNAL OF COASTAL AND HYDRAULIC STRUCTURES

Vol. 1, 2021, 6

Field measurements of very oblique wave run-up and overtopping with laser scanners

Patrick Oosterlo[1], Bas Hofland[2], Jentsje W. van der Meer[3], Maarten Overduin[4], and Gosse Jan Steendam[5]

Abstract

This paper presents the first field measurements with an innovative laser scanner system, during a severe winter storm. The goal of this paper is to validate this system for measuring wave run-up and wave overtopping parameters during storms with very oblique wave attack. To this end, the paper describes the analysis of the data obtained during storm Ciara (10 - 12 February 2020) and validates the results with data from overtopping tanks and video recordings. Storm Ciara was a highly unique and complex storm, with offshore-directed wind and alongshore-directed waves at the dike. This posed large challenges for measuring the front velocities.

The wave run-up heights and the overtopping discharges could be measured accurately with the laser scanners. Reasonable results were achieved for the run-up depths. This has led to several new insights into the probability distribution of oblique wave run-up and the run-up depths of up-rushing oblique waves. The 2D front velocities that were derived from laser data deviated more from a commonly used equation. The wave angle of incidence could not be determined as accurately for storm Ciara, as in previous calibration tests and numerical simulations with less oblique wave attack. This arose from the very oblique wave attack during storm Ciara.

Keywords

Laser scanner, LIDAR, field measurements, oblique wave attack, wave run-up, wave overtopping, dike

[1]P.Oosterlo@tudelft.nl, Delft University of Technology, Delft, The Netherlands
[2]B.Hofland@tudelft.nl, Delft University of Technology, Delft, The Netherlands
[3]jm@vandermeerconsulting.nl, Delft University of Technology, Delft, The Netherlands; Van der Meer Consulting BV, Akkrum, The Netherlands; IHE Delft, Delft, The Netherlands
[4]maarten.overduin@infram-hydren.nl, Infram Hydren, Maarn, The Netherlands
[5]gosse.jan.steendam@infram-hydren.nl, Infram Hydren, Maarn, The Netherlands

This paper was submitted on 12 May 2021. It was accepted after double-blind review on 2 August 2021 and published online on 1 September 2021

DOI: https://doi.org/10.48438/jchs.2021.0006

Cite as: "Oosterlo, P., Hofland, B., Van der Meer, J., Overduin, M., Steendam, G. J. (2021). Field measurements of very oblique wave run-up and overtopping with laser scanners. Journal of Coastal and Hydraulic Structures, 1. https://doi.org/10.48438/jchs.2021.0006"

The Journal of Coastal and Hydraulic Structures is a community-based, free, and open access journal for the dissemination of high-quality knowledge on the engineering science of coastal and hydraulic structures. This paper has been written and reviewed with care. However, the authors and the journal do not accept any liability which might arise from use of its contents.

1 Introduction

Wave run-up and wave overtopping measurements in the field are scarce, since they are very difficult to perform. Wave run-up is typically measured in the field using step gauges (e.g. Wenneker et al., 2016). Other techniques, such as stereo-photogrammetry (e.g. De Vries et al., 2011), ultrasonic altimeters (e.g. Matias et al., 2014) and video recordings (e.g. Vousdoukas et al., 2012) have also been used. More recent studies (e.g. Brodie et al., 2012; Vousdoukas et al., 2014) used terrestrial laser scanners (LIDARs) to measure the wave run-up in the field as well. Wave overtopping measurements in the field are performed even less. Recently, a 3D mesh of capacitance wires was used in an attempt to measure wave overtopping in the field (Pullen et al., 2019).

However, typically wave overtopping measurements in the field are performed using overtopping tanks (e.g. De Rouck et al., 2009; Van der Meer et al., 2019; Wenneker et al., 2016). This is a robust method to measure wave overtopping, but fixed at each location and at a fixed elevation.

Oosterlo et al. (2019, 2021) developed an alternative innovative and more flexible solution, using two terrestrial laser scanners. They showed that the system can measure the run-up heights, run-up depths (flow depths, layer thicknesses) and front velocities of up-rushing waves on a dike in field situations with oblique wave attack. From these measurements, also the virtual wave overtopping can be calculated at any height level. Furthermore, an estimate of the (peak) wave period and angle of incidence can be obtained from the data. Determining these two parameters from the run-up signals could alleviate the need for additional measurements offshore. Another advantage of the system is that more insight is gained into certain parameters than with the conventional measurement techniques, e.g. into the depths and velocities, which are measured with high resolution. Since the system is mobile, it can be used to measure at several dike locations by moving the system every few years. The present paper builds on the system calibration of Oosterlo et al. (2019, 2021).

An extensive field measurement project is being performed in the Eems-Dollard estuary in the north of the Netherlands for a period of 12 years. The measurements started in 2018, measuring wind, water levels, waves, wave run-up and overtopping. The estuary consists of deep channels and shallow tidal flats and is part of the Wadden Sea, a shallow shelf sea (see the left panel of Figure 1). A particular aspect for this area is that the dike design conditions consist of very obliquely incident waves, up to 80° relative to the dike normal. As the reliability of the models as used for the Dutch dike safety assessment has not been sufficiently validated for such conditions, the aim of the measurements is twofold. First, to understand the processes yielding nearshore wave conditions better, ultimately leading to improved numerical prediction models. Second, to understand the processes related to oblique wave run-up and overtopping better, leading to improved prediction methods. In the project, the wave overtopping discharge is measured with four wave overtopping tanks built into dikes at two locations.

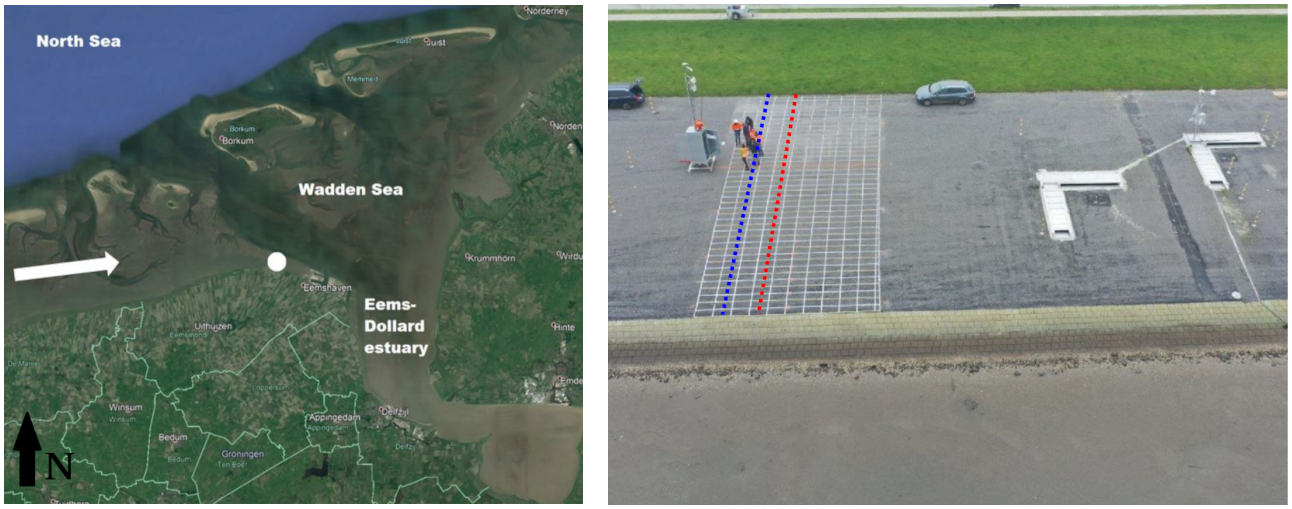

(a) Eems-Dollard estuary, area of interest.

(b) Measurement location.

Figure 1: Left: The Eems-Dollard estuary in the Netherlands, area of interest of the field measurement project. Laser scanner system location indicated by white dot. Wind direction during storm Ciara indicated with the arrow. Satellite image: ©2021 GeoBasis-DE/BKG, ©2021 Google. Data: SIO, NOAA, U.S. Navy, NGA, GEBCO. Right: Drone overview of measurement location, with the laser scanner pole (left), the approximate laser scan line locations (blue and red dashed lines), the painted grid on the slope, and two of the overtopping tanks (right).

The laser scanner system of Oosterlo et al. (2019, 2021) has been updated and upgraded, and is now placed next to two of the overtopping tanks on the dike in the Eems-Dollard estuary, to measure during actual severe winter storms. Previous research measuring wave run-up in the field using laser scanners often used only one laser scanner with a low temporal resolution. To the best of the authors' knowledge, this is the first time that a system using two laser scanners is used to measure these directional parameters in the field, with a high resolution, and during an actual storm with very oblique wave attack.

The goal of this paper is to validate this innovative system for measuring wave run-up and wave overtopping parameters during an actual severe winter storm with very oblique wave attack. To this end, the present paper describes the analysis of the data obtained during storm Ciara (10 - 12 February 2020) and validation with data from the overtopping tanks and video recordings. Furthermore, the paper compares the data as gathered during storm Ciara to the current knowledge on wave overtopping, to gain new insights in the influence of very oblique wave attack on wave overtopping.

The outline of this paper is as follows. First, the set-up of the new system is described briefly. After that, section 3 gives a short description of the measured storm. The next section describes the methods, split into the system calibration, the data processing and the data analysis. This is followed by the results and validation of the measured parameters in section 5. The final section gives the conclusions and presents an outlook on the next steps in this research program.

2 System set-up

Oosterlo et al. (2019, 2021) described the first version of the laser scanner system. Recently, an updated version of the system was developed, now using a retractable vertical pole in a cabinet instead of a tripod perpendicular to the dike slope. In October 2019, the new system was placed on the dike at Uithuizerwad in the Eems-Dollard estuary, next to two of the overtopping tanks. See the right panel of Figure 1 and Figure 2 for an overview of the measurement location and the system set-up. The retractable pole and cabinet make the system easier to place, set-up and relocate. The waterproof cabinet also contains all the auxiliary devices for the connection of the instruments and the data storage. The present system uses two SICK LMS511pro HR laser scanners, cost-efficient laser scanners with a near-infrared (905 nm) laser beam, which is the newest version of a commonly used laser scanner in previous research (e.g. in Hofland et al., 2015; Streicher et al., 2013). Also, a camera with a framerate of 50 fps is attached to the pole, to further validate the run-up heights and front velocities, see the right panel of Figure 2. Furthermore, an accelerometer is attached to the upper laser scanner, to be able to correlate possible outliers with vibrations of the system. The laser scanners measure both the distance R [m] to a surface and the reflected signal intensity RSSI [-] (Received Signal Strength Indicator, a dimensionless value between 0 and 255), which provides information on the type of surface. The scanners have a sampling frequency of 50 Hz, an angular resolution of 0.333°, are synchronised, and detect the last out of five echoes, to reduce the influence of e.g. rain on the data, see Oosterlo et al. (2019). The two laser scanners each scan a line parallel to each other, running from the dike toe to the crest (blue and red dashed lines in the right panel of Figure 1). To aid with the video analysis, a 20 m x 10 m grid with a resolution of 0.5 m by 1 m was painted on the slope, also refer to the right panel of Figure 1 and the left panel of Figure 2.

The local dike slope consists of concrete blocks up to approximately 2 m+NAP (Normaal Amsterdams Peil, Dutch ordnance level, roughly corresponding to mean sea level), asphalt from 2 m+NAP until 6.6 m+NAP and grass from 6.6 m+NAP until approximately 9 m+NAP. The average dike slope at the measurement location is 1:4.5. The cabinet with the laser scanner pole was placed on the asphalt slope at a height of 5 m+NAP. The laser scanners are located at heights of 5.55 m and 6.04 m above the slope, hence at 10.55 m+NAP and 11.04 m+NAP. The distance between the laser scan lines is 1.97 m, which is the optimal spacing (Oosterlo et al., 2021). The resulting slant angles (ϕ_1 and ϕ_2 in Figure 7) are 26.0° and 37.6°.

The overtopping tanks are placed inside and flush with the dike slope (see the right panel of Figure 1 and Figure 3) and collect water through thin openings at elevations of 4.4 m+NAP and 5.3 m+NAP. The tanks are approximately 0.8 m deep and 1.3 m wide, and have a 4 m-wide opening for entering by overtopping waves. The collected volume of water in the tanks is monitored by measuring the water level in the tanks by pressure transducers, and the water can flow out freely through a gate in an outflow channel (Van der Meer et al., 2019).

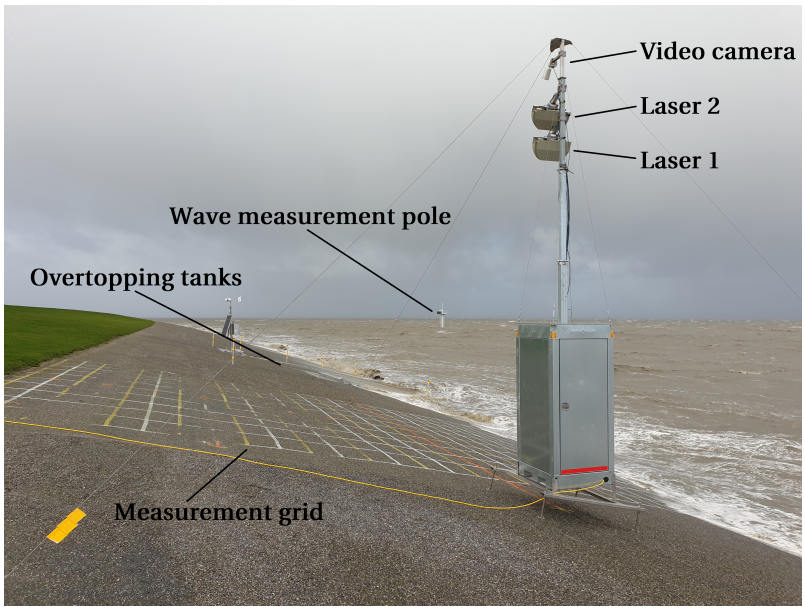

(a) Measurement instruments.

(b) Zoom of laser scanner system.

Figure 2: Left: New laser scanner system on the dike in the Eems-Dollard estuary, next to the overtopping tanks, during storm Ciara. The Rijkswaterstaat (wave) measurement pole can be seen in the distance. Rijkswaterstaat is the Directorate-General for Public Works and Water Management in the Netherlands. Right: From the bottom to the top, Laser scanner 1, laser scanner 2, video camera.

Figure 3: Excavation of the dike slope and placement of the overtopping tanks inside the dike.

3 Measurements during storm Ciara

The focus of this paper lies on the measurements performed during storm Ciara. Storm Ciara was an extratropical cyclone, which hit large parts of northern Europe starting on 7 February 2020. Measurements were performed from 10-02-2020 to 12-02-2020. Even though the largest wind velocities occurred on 9 February, the south-southwestern wind direction as present on the 9$^{\text{th}}$ did not lead to large water levels or wave heights at the location of interest. This is due to the orientation of the location of interest (see the left panel of Figure 1). From 10 to 12 February, the wind direction ranged between west-southwest and west. During these three days, the maximum measured average wind velocity was 21 m/s, the maximum water level h was 3.03 m+NAP, the maximum significant wave height H_{m0} was 0.97 m and the corresponding wave peak period T_p was 4.35 s, also see Table 1. Note the unusual ratio of $T_p/T_{m-1,0}$. For a JONSWAP spectrum, this ratio is approximately 1.1. Here, it was approximately 0.9, which indicates a non-standard spectral shape.

The laser scanner system was previously tested for normally and obliquely incident bores (Oosterlo et al., 2019, 2021). Ciara was the first actual storm that was measured with the system, and immediately tested it to the extreme. Ciara was a highly unique storm, with offshore-directed wind at the measurement location and waves that refracted somewhat to the shallow flats in front of the dike to become almost alongshore-directed waves at the dike, see Figure 4. Thus, Ciara caused highly complex conditions at the measurement location with very oblique wave attack with angles of incidence of approximately 70° and more. This poses large challenges for measuring and even just defining, e.g. the 2D front velocities and the overtopping volumes and discharges, also see Figure 5. Furthermore, the offshore-directed wind and very obliquely incident waves led to few overtopping waves (≈50) and therefore a small overtopping discharge (≈0.1 l/s/m) in the lower overtopping tank at 4.4 m+NAP.

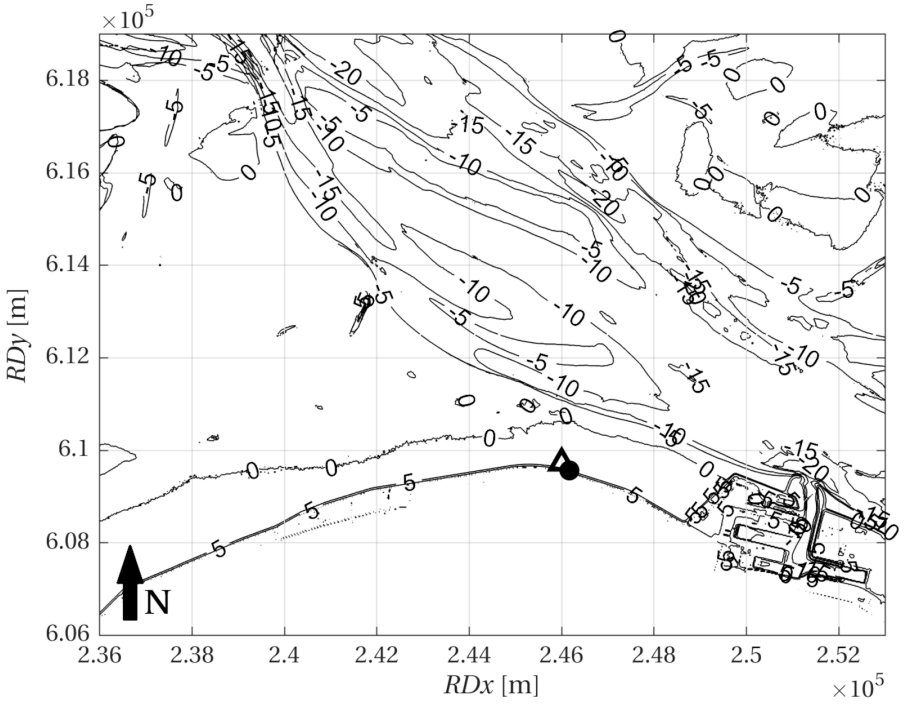

Figure 4: Bathymetry of the area of interest, shown as depth contours [m+NAP], with the deep main tidal channel and shallow flats in front of the dike. Laser scanner system (circle) and measurement pole (triangle) locations indicated.

Since the tide at the location of interest is semidiurnal, from 10 to 12 February five high tides were measured. During two of these five high tides more than one wave entered the lower wave overtopping tank. Therefore, these two high tides were selected for further analysis, and from these two high tides two storm peak periods were derived. Table 1 and Figure 6 present the characteristics of the two storm peaks. Note the positive correlation between water level and wave height, due to the depth-limited conditions at the measurement location.

Run-up heights and depths and 2D front velocities as measured by the laser scanners during storm Ciara

Table 1: Characteristics of considered storm peaks. W_{dir} [°N] is the wind direction, W_{vel} [m/s] the wind velocity, h [m+NAP] the water level, d [m] the water depth, $H_{1/3}$ [m] the significant wave height based on the time signal, H_{m0} [m] the significant wave height based on the spectrum, $T_{1/3}$ [s] the significant wave period based on the time signal, T_{p} [s] the peak wave period, $T_{\mathrm{m\text{-}1,0}}$ [s] the wave period based on the moments of the spectrum, δ [°N] the mean wave direction, β [°] the wave angle of incidence relative to the dike normal, q_{tank} [l/s/m] the overtopping discharge as measured by the overtopping tank, N_{ow} [-] the number of overtopping waves in the overtopping tank. RWS pole is the Rijkswaterstaat (wave) measurement pole, see the left panel of Figure 2.

	Storm peak 1	Storm peak 2	Data source
Date	10-02-2020	11-02-2020	
Start time	11:20	23:50	
Duration [hh:mm]	1:00	1:20	
W_{dir} [°N]	265	260	RWS pole (wind direction meter)
W_{vel} [m/s]	18.5	15.0	RWS pole (wind velocity meter)
h [m+NAP]	2.93	3.03	RWS pole (floater)
d [m]	2.38	2.48	RWS pole (floater)
$H_{1/3}$ [m]	1.00	0.95	RWS pole (radar)
H_{m0} [m]	0.97	0.90	RWS pole (radar)
$T_{1/3}$ [s]	4.2	4.15	RWS pole (radar)
T_p [s]	4.35	4.00	RWS pole (radar)
$T_{m-1,0}$ [s]	4.95	4.65	RWS pole (radar)
δ [°N]	312	311	Equation 1
β [°]	66	67	Equation 1
q_{tank} [l/s/m]	0.130	0.107	Wave overtopping tank
N_{ow} (tank) [-]	57	55	Wave overtopping tank

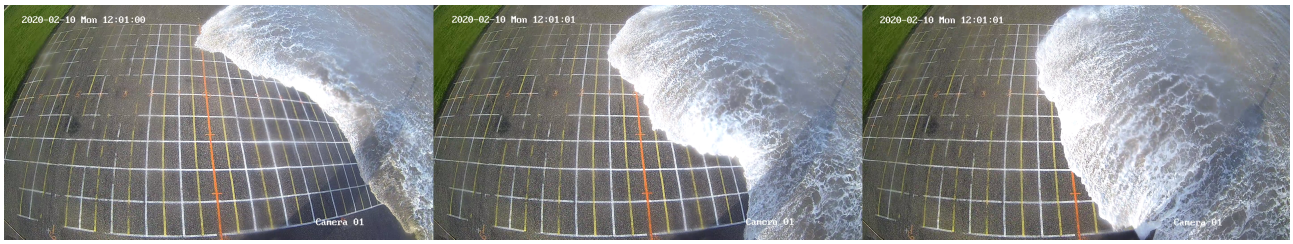

Figure 5: Three snapshots taken from the video recordings, showing a very oblique wave running up the slope in a sort of local plunging motion. Note the painted grid as used for the video analysis.

were compared to analysed video recordings and the EurOtop (2018) equations. The (virtual) wave overtopping discharge, as determined from the laser data, was compared to overtopping data from the overtopping tank and the EurOtop (2018) equations. Estimates of the peak wave period were compared to local radar measurements, see Table 1. Note that the mean wave direction and angle of incidence were not measured directly, but based on a relation between the mean wind direction and mean wave direction, which was derived based on previous measured storms in the area (Van der Meer, 2018):

$$\delta = 230^\circ + 0.31 * W_{dir} \tag{1}$$

where δ [°N] is wave direction at the measurement location and W_{dir} [°N] is the wind direction at the measurement location. The accuracy of the mean wave direction and thus angle of incidence is estimated to be approximately ±5°. A short video overview of the measurements can be found at `https://youtu.be/JrItZ58u6gU`.

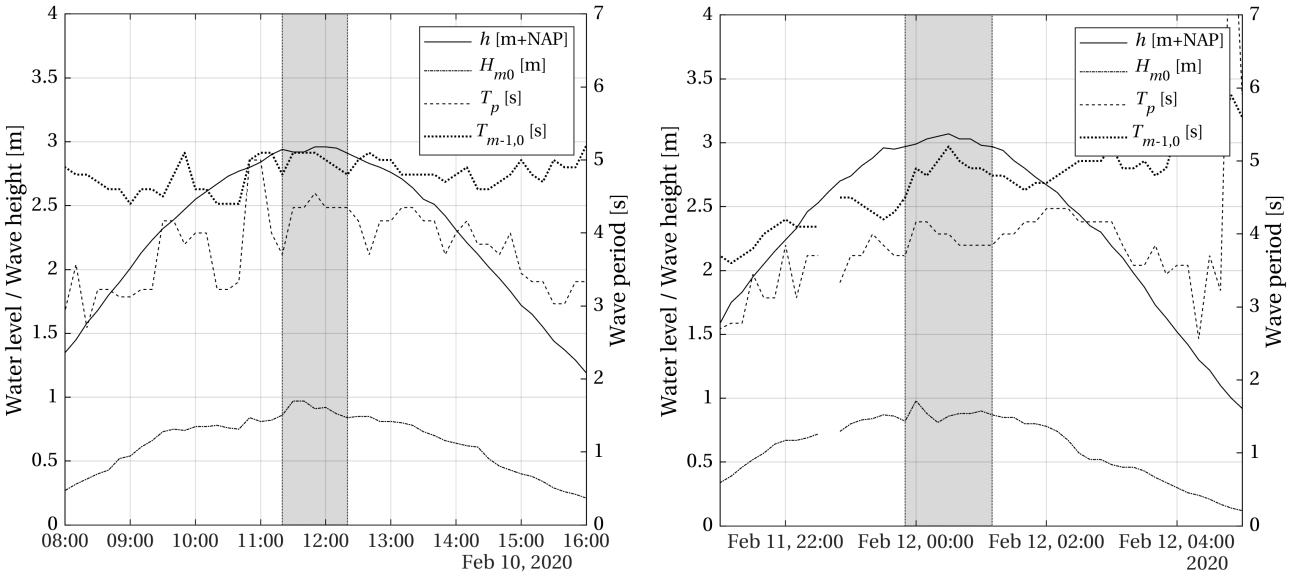

(a) Storm peak 1.

(b) Storm peak 2.

Figure 6: Overview of measurements near the toe of the dike around both storm peaks. The shaded regions indicate the considered storm peaks. h [m+NAP] is the water level, H_{m0} the significant wave height [m], T_{p} the peak wave period [s], $T_{\mathrm{m\text{-}1,0}}$ [s] the wave period based on the moments of the spectrum.

4 Methods

Oosterlo et al. (2019, 2021) described the calibration and data processing procedures extensively. The same calibration procedures were followed here. With the new version of the laser scanner system, the data processing procedures were updated compared to Oosterlo et al. (2019, 2021) related to several aspects. The measured distances R [m] in polar coordinates were now transformed to x, z and a-coordinates according to Figure 7. The x and z-coordinates can be determined directly from the measured distances for a vertical pole, by using:

$$x = x_s + R\sin\theta \tag{2}$$

$$z = z_p + h_s - R\cos\theta\cos\phi \tag{3}$$

with z [m] being the z-coordinate, x [m] the x-coordinate, x_s [m] the x-coordinate of the laser scanner, z_p [m] the z-coordinate of the laser scanner pole [m], h_s [m] the height of the laser scanner above the slope, R [m] the measured distance, θ [°] the scan angle and ϕ [°] the slant angle. Generally, a dike slope is not straight, but convex. Furthermore, slight errors in the mounting and orientation of the laser scanners can occur. To account for this, a rotation matrix was applied to the calculated coordinates:

$$M = \begin{bmatrix} \cos\psi & -\sin\psi \\ \sin\psi & \cos\psi \end{bmatrix} \tag{4}$$

The correction angle ψ [°] rotates the x- and z-coordinates in the x,z-plane, see Figure 7. ψ was determined by fitting the x and z-coordinates resulting from the rotation matrix to the GPS-measured dike slope. The final maximum difference in x-coordinate between the GPS-measured dry slope and the dry slope as calculated from the laser data was 0.04 m, the same order of magnitude as the scan resolution and laser footprint. The maximum difference in z-coordinate between GPS and lasers was 0.05 m, which can be considered accurate, given the convex and irregular shape of the dike slope, the accuracy of the GPS and the maximum accuracy of the mounted laser scanners. The run-up depths can be determined with a higher accuracy. This can be explained as follows: the error in the measurements of the dike slope and water surface is constant. Since the difference between the solid dike slope and the water surface is determined, this error will cancel out. The along-slope a-coordinates were then determined from the x and z-coordinates by using Pythagoras' theorem.

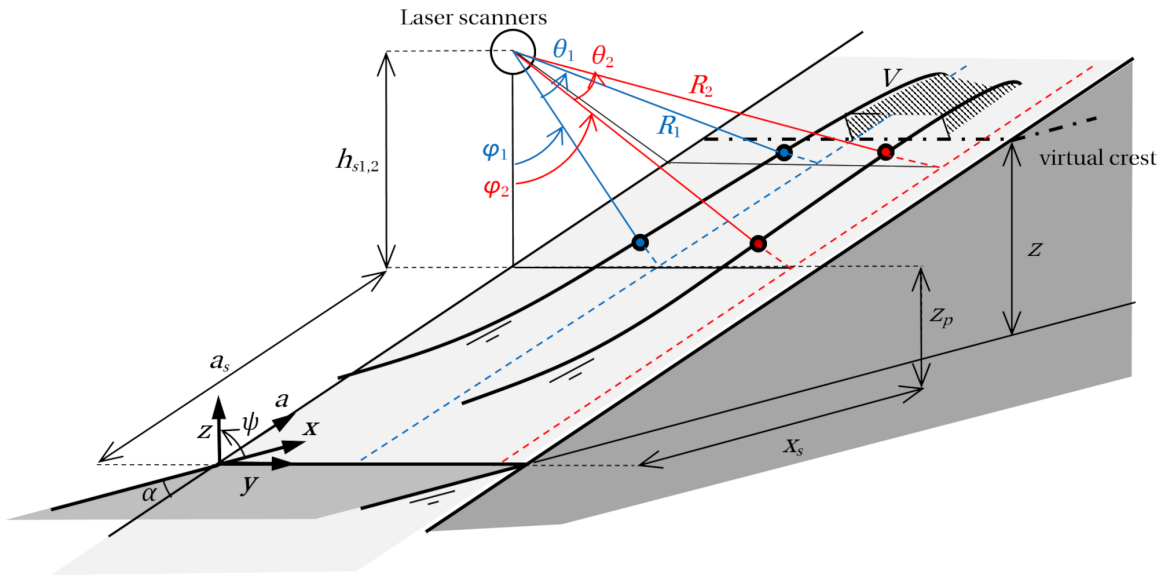

Figure 7: Schematised updated set-up with two laser scanners. Scan lines (red and blue dashed lines), scanned points on water surface (red and blue dots) are indicated. x (horizontal), y (perpendicular), z (vertical) and a-coordinate (along the slope) system is also indicated. $R_{1,2}$ [m] are the scanned distances, $\theta_{1,2}$ [°] are the scan angles, $\phi_{1,2}$ [°] the slant angles, x_s [m] are the x-coordinates of the laser scanners, a_s [m] the a-coordinates of the laser scanners, z_p [m] is the z-coordinate of the laser scanner pole, $h_{\mathrm{s}1,2}$ [m] are the heights of the laser scanners above the slope, α [°] is the slope angle. V [m^3] is a virtual overtopping volume, ψ [°] is the correction angle resulting from the rotation matrix, rotating the x- and z-coordinates in the x,z-plane.

As described in Oosterlo et al. (2019, 2021), the percentage of invalid point measurements at a certain location indicates the quality of the measurement. An invalid measurement means that the magnitude of the laser reflection was too small. These percentages were very low (of order 0.1%), hence overall the data quality was very good.

After interpolating the data and applying median filters (refer to Oosterlo et al., 2019), the run-up depths were determined by subtracting the dry slope surface from the measured surface at a certain moment. Run-up depths smaller than a certain threshold, depending on the data quality of the specific laser scanner and storm peak, were removed to remove noise from the signal and prevent the detection of unrealistically high run-up values. Noise in the signal can be caused by e.g. the laser beam reflecting off raindrops, slight inaccuracies in the mounting and orientation of the laser scanners, and the accuracy of the laser scanners themselves, which is in the order of 0.01 m. The threshold is chosen in such a way that realistic and accurate run-up depths and heights are obtained (as verified with video recordings), without extreme outliers. 0.015 m was used for laser scanner 1, 0.030 m and 0.020 m were used for laser scanner 2 for storm peak 1 and 2, respectively. The data were then further corrected by removing depths larger than 1.5 m, and by removing large (>0.5 m) local (in one time or space step) differences in run-up depths, e.g. caused by rain. If an isolated (non-NaN) run-up depth was measured higher on the slope after more than 10 connected invalid measurement points (NaN values), these values were also removed, as they were caused by noise in the data. A similar procedure was followed for the reflectance value, RSSI: a large difference (>100) in one time or space step was removed, a threshold value (1 - 5) was used to prevent unrealistically high run-ups, and valid values after 10 or more straight NaNs were removed.

The wave run-up heights, wave overtopping volumes and discharges, and wave peak periods and angles of incidence were determined in the same way as in Oosterlo et al. (2019, 2021), where the full descriptions can be found. Briefly, this means that for the run-up the highest location on the slope was determined where $z_{\text{run-up}} - z_{\text{dry}} > z_{\text{threshold}}$ or $\text{RSSI}_{\text{run-up}}$-$\text{RSSI}_{\text{dry}} > \text{RSSI}_{\text{threshold}}$. Overtopping volumes and discharges were found by integrating the run-up depths between a certain virtual crest level and the run-up level, and then determining the maximum volumes per wave. Wave peak periods were calculated from the variance density spectra of the run-up time signals. The angle of incidence was then determined based on the cross-spectral density of both run-up time signals.

The front velocities were determined from the temporal change in run-up level. To this end, first the time signal of the instantaneous front position was smoothed by applying a median filter with a 0.2 s window, followed by a moving average with a 0.4 s window. After that, the time derivative was taken and the maxima were determined, giving the maximum front velocities during each wave. To validate the laser data, the front velocities were also determined from the videos; by taking the number of video frames it took the front to travel 0.5 m (a somewhat coarser approach).

Estimates of the displacements of the laser lines due to wind vibrations were calculated from the accelerometer data, to be able to correlate possible outliers in the laser data.

Mentaschi et al. (2013) showed that the root-mean-square error RMSE and its variants give smaller values for models affected by negative bias. Hence, these indicators are not always reliable to assess the accuracy of models or measurements. They showed that the HH-indicator as proposed by Hanna and Heinold (1985) provides more reliable information on the accuracy. This HH-indicator was used in Oosterlo et al. (2021) and the present paper also uses this indicator. It is defined as:

$$HH = \sqrt{\frac{\sum_{i=1}^{N} (M_i - O_i)^2}{\sum_{i=1}^{N} M_i O_i}} \tag{5}$$

where M_i is the ith modelled data, O_i is the ith observation and N is the total number of observations. Furthermore, the Normalised Bias Indicator is used:

$$NBI = \left(\overline{M} - \overline{O}\right) / \overline{O} \tag{6}$$

Both the HH and NBI are dimensionless. These indicators are used to determine the accuracy of the measured laser data, by comparing them to data measured by other instruments and several equations.

5 Results

5.1 Wave run-up heights

Figure 8 presents a typical part of the measured data, showing the run-up signals based on both measured distance R and laser reflectance RSSI for both laser scanners, during a 30-second window. The figure shows the run-up peaks and measured run-up depths as well. The height level of the overtopping tank is indicated with the dotted line. One of the waves shown in the figure caused overtopping in the overtopping tank. Furthermore, the slight delay between the laser scanner signals is visible, where the waves often reached the second laser scanner first with the present wave direction.

Figure 9 shows the measured run-up heights for both storm peaks, plotted against the run-up heights observed from the video recordings. The figure shows the run-up heights for both laser scanners, based on both the measured distance R and laser reflectance RSSI data. Figure 9 only shows the run-up heights above 4.4 m+NAP, hence the most important waves, as these are the waves that would give overtopping in the overtopping tank. Similar trends were also found for the smaller run-up heights. Note that different numbers of run-up events above the threshold run-up height were found with both laser scanners and the video analysis; due to the very obliquely incident waves, some of the waves reached the threshold run-up height at the location of one of the laser scanners, but not at the other one. These numbers of run-up events and the $R_{u2\%}$-values have been given in Table 2.

Some general observations for both storm peaks can be made. The first one is that both laser scanners generally performed well, as the run-up heights agree quite well with the values as observed from the videos, also visible in the HH and NBI values. Second, the run-up heights based on the measured distances agree better with the video data than the run-up heights based on the RSSI. The RSSI performed quite well for the first storm peak with a few outliers, but gave larger HH and NBI-indicator values for the second storm peak, underestimating the run-up heights. Previous studies Cete (2019); Hofland et al. (2015); Oosterlo et al. (2019, 2021) found that the RSSI performed equal to or better than the measured distance. This can be explained as follows: the RSSI analysis is based on the difference in reflectance between the dry slope and the up-rushing water. The asphalt gives a low reflectance, the water a higher one. However, the paint of the grid on the slope was very reflective. This thus led to large RSSI values at the grid lines, interfering with the higher RSSI values of the up-rushing waves. This reduced the quality of the present RSSI results.

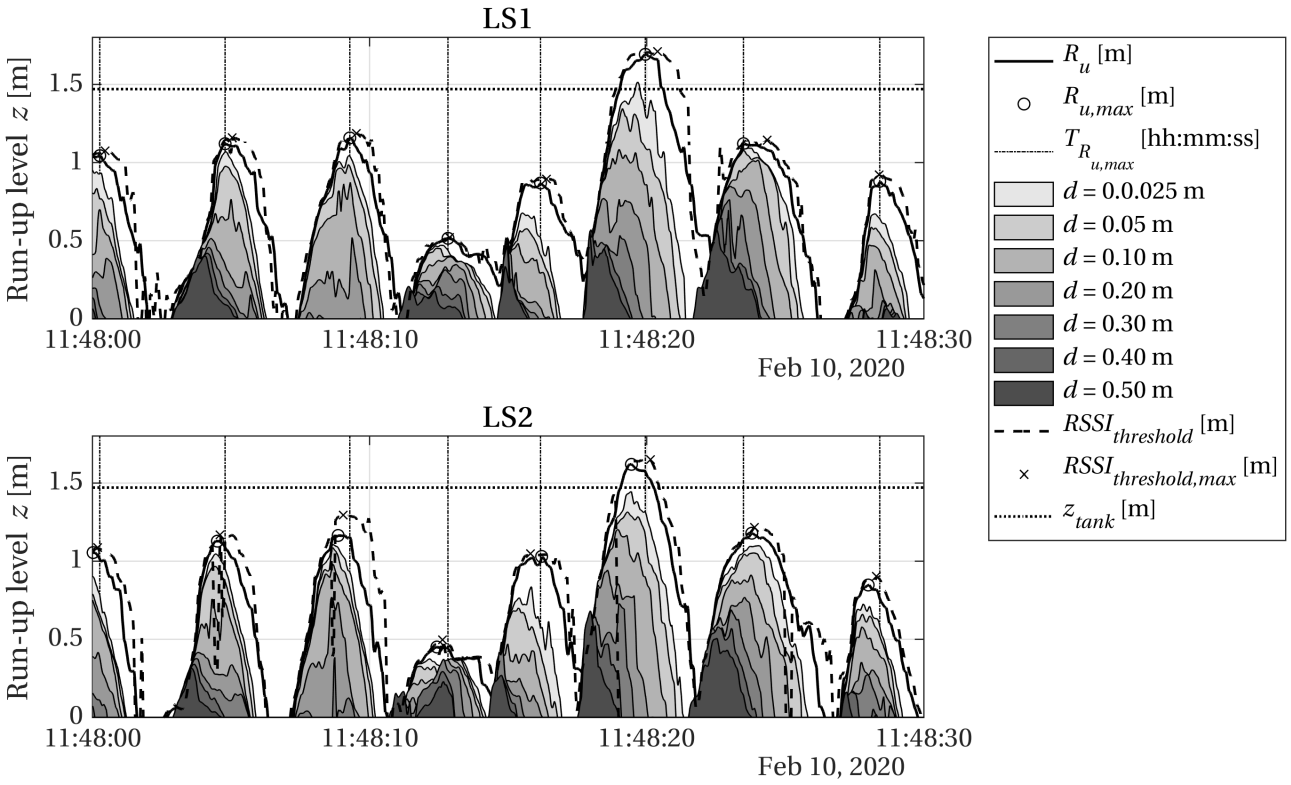

Figure 8: Measured run-up heights R_u [m] based on measured distances R (solid lines) and laser reflectance RSSI (dashed lines), as well as measured run-up depths d [m] (contours) for both laser scanners (LS1 and LS2), during a 30 second window. Maximum run-up heights $R_{u,max}$ [m] per wave based on both R (circles) and RSSI (crosses) indicated. Height level of the overtopping tank z_{tank} [m] indicated by the dotted line. Moments of maximum run-up height $T_{R_{u,max}}$ [hh:mm:ss] at LS1 indicated by the dash-dot lines. Note the delay between the signals, where the waves often reached LS2 first with the present wave direction.

Also, some storm peak-specific observations can be made. The run-up heights of peak 1 agree well, especially based on the measured distances of laser scanner 1, with almost all values within the ±0.10 m bounds. Absolute HH and NBI values are at most 0.05, where the run-up based on measured distances shows a slightly negative bias, and the RSSI-based values show a bias close to zero. As the accuracy of the video analysis is estimated to be a_{Ru}±0.10 m (z_{Ru}±0.02 m), this means that the differences are of the same order of magnitude as the accuracy of the video analysis. The results of laser scanner 2 for storm peak 1 (HH = 0.05, NBI = -0.02) show somewhat larger deviations than the results of laser scanner 1 (HH = 0.02, NBI = -0.02). Since the second laser scanner scans a line further from the pole, the measured distances and laser footprint are larger, whereas the laser resolution is lower than of laser scanner 1. Therefore, the data quality of the second laser scanner was somewhat lower and the deviations somewhat larger.

During the analysis, it was observed that the largest deviations of the first storm peak occurred from 11:30 until 11:36, when wind gusts were strongest, which caused stronger vibrations of the system. The accelerometer data were analysed, and the largest displacements of the scan lines indeed occurred between 11:30 and 11:36, being at most a displacement of 0.09 m along the y-axis (see Figure 7) for laser scanner 2. As the y-axis roughly corresponded to the wind direction, displacements along the a-axis were much smaller. These wind vibrations were also visually observed during the measurements. Therefore, the guywires of the system were tightened more after the first storm peak, to reduce the vibrations during the measurements of the next storm peaks. By doing this, they were reduced to at most 0.06 m in the y-direction for the following storm peaks.

Results based on measured distances also agree well for the second storm peak, showing again a slight negative bias. However, for this storm peak the results based on the RSSI do not agree well at all. Additional to the influence of the painted grid lines, a period of strong wind combined with very heavy rain occurred on 12-02-2020 from 00:34 until 00:37. As described in Oosterlo et al. (2019), the influence of raindrops on the data quality is small when the last echo is used for the laser scanner measurements. This explains the good results

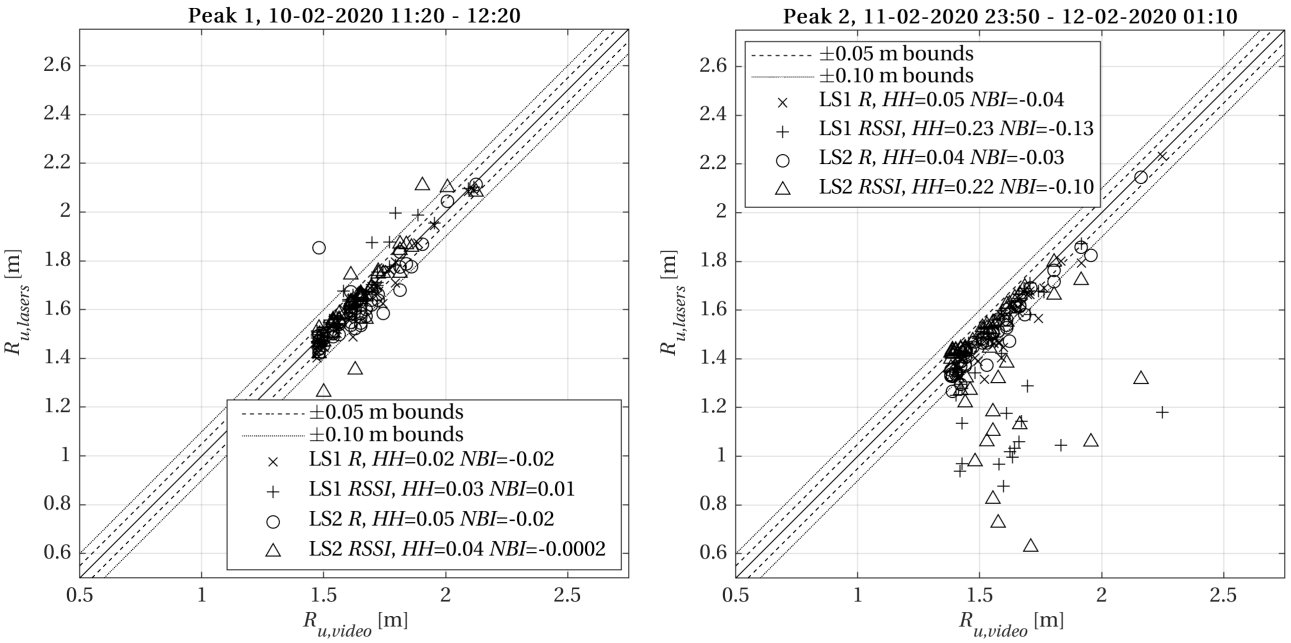

(a) Storm peak 1.

(b) Storm peak 2.

Figure 9: Run-up heights above 4.4 m+NAP for both storm peaks for both laser scanners (LS1 and LS2), based on distance R and laser reflectance RSSI, compared with run-up heights from video recordings. Left: storm peak 1. Right: storm peak 2. The legend provides the HH and NBI values.

of the distance-based run-up heights, despite the rain. However, the combination of strong wind and heavy rain caused raindrops to fly past the laser scanners continuously, whereby the laser beam sometimes reflected off the raindrops, detecting a 'water-like' higher reflectance (RSSI) value, when no water was present on the slope. The combined effects of the painted grid lines and very heavy rain thus led to a larger RSSI threshold being necessary during the analysis. This then led to upper parts of the up-rushing waves being filtered out, reducing the RSSI-based data quality. Therefore, the remainder of this paper will only consider the results based on measured distances. However, note that an extreme value analysis fit through the largest RSSI events would also still be accurate.

The left panel of Figure 10 compares the $R_{u2\%}$, the run-up height exceeded by 2% of the waves, based on the laser scanner data of both storm peaks, to the Van der Meer and Bruce (2014) wave run-up equations, which were later implemented in EurOtop (2018) (and hereafter referred to as such). Note that the influence of oblique wave attack was added to the equations here, by including the influence factor γ_β [-] on the vertical axis. The value of γ_β is 0.85 for the run-up, for the present angles of incidence of 66° and 67°. A dike slope angle of 1:4.2 was used, which is the average slope of the asphalt section of the dike. The data of both storm peaks lie closely together (a result of the similar conditions during both peaks) and fall just above the lower 90%-bound of the EurOtop (2018) equations. EurOtop (2018) gives a 25% larger $R_{u2\%}$, see Table 2. However, note that the results are quite sensitive to changes in the angle of incidence and especially the $T_{m-1,0}$ wave period, on which the breaker parameter $\xi_{m-1,0}$ [-] is based. As explained in section 3, there exists some uncertainty in the mean wave direction and thus in the angle of incidence, since they were not measured directly, but based on a relation between the wind direction and wave direction. There is also some uncertainty in the $T_{m-1,0}$. A difference in angle of incidence of 5° or a more commonly found ratio of $T_p/T_{m-1,0} = 1.1$, would move the data from the lower 90%-bound to the upper one in Figure 10. This highlights the importance of accurately measuring these parameters.

The right panel of Figure 10 plots the exceedance probability distributions of the measured run-up heights for both laser scanners and storm peaks on Weibull scale. Here, $P\left(R_{u,i} \geq R_u\right)$ [-] is the probability that a certain run-up height $R_{u,\mathrm{i}}$ [m] exceeds a specified run-up height R_u [m]. The complementary cumulative distribution function or exceedance function of the Weibull distribution is:

$$P\left(X \geq x\right) = e^{-\left(\frac{x}{a}\right)^b} \tag{7}$$

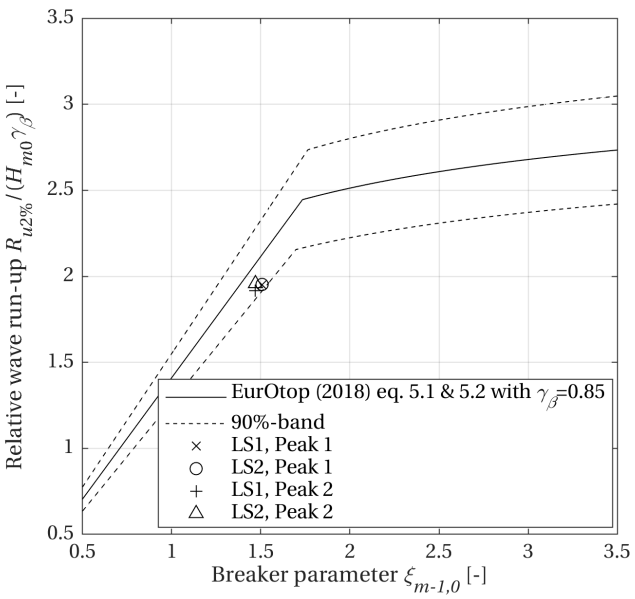

(a) Relative wave run-up.

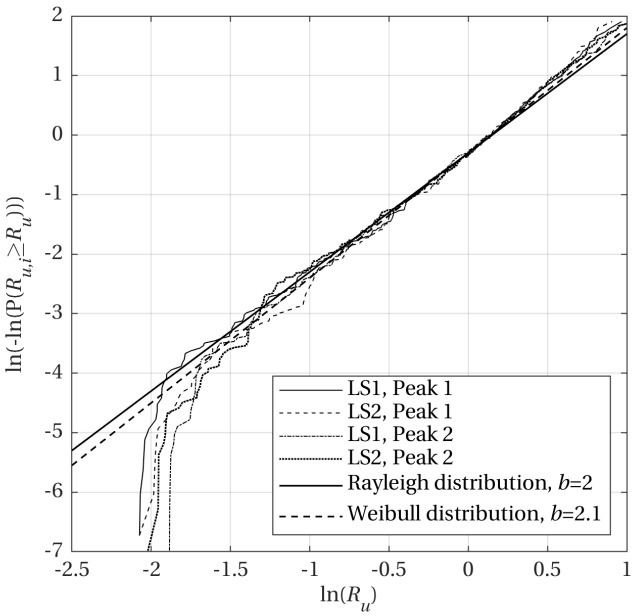

(b) Run-up exceedance.

Figure 10: Left: Relative wave run-up versus breaker parameter. Figure based on EurOtop (2018). Note the added influence of the oblique wave attack on the vertical axis compared to EurOtop (2018). Data for both laser scanners based on measured distances, and for both storm peaks. Right: Run-up exceedance plots for both laser scanners and both storm peaks, plotted on Weibull scale. A straight line gives a Weibull distribution, a straight line with a slope of 1:2 gives a Rayleigh distribution.

where $\mathrm{P}(X \geq x)$ is the probability that X is equal to or larger than x [-], b is a non-dimensional shape factor and a is a dimensional scale factor of the distribution. The data have a Weibull distribution if the data show as a straight line in the right panel of Figure 10. Deep water waves are Rayleigh-distributed, the Rayleigh distribution is essentially a Weibull distribution with a shape factor b of 2. E.g. Nielsen and Hanslow (1991) determined that the run-up heights on a beach for normally incident waves in deep water also have a Rayleigh distribution. When waves approach shallow water and the highest waves break, the wave height distribution, which first could be described by a Rayleigh-distribution (Weibull distribution with $b = 2$), turns into a Weibull distribution with $b > 2$ (Battjes and Groenendijk, 2000; EurOtop, 2018) or other function with decreased magnitude of low-exceedance events (e.g. Battjes and Groenendijk, 2000). Van der Meer and De Waal (1993) found that if the wave height distribution deviates from a Rayleigh distribution due to shallower water, then the run-up distribution will also deviate with approximately the same amount. The run-up distribution will then also turn into a Weibull distribution with $b > 2$ (Stam, 1989). Stam (1989) also found that the run-up remains approximately Rayleigh-distributed for deep water conditions with limited depth-induced breaking ($d_{toe}/H_{s,toe} \geq 2$ or 3), for rubble mound slopes. The exact run-up distribution on a dike slope of (very) obliquely incident deep or shallow water waves is unknown. However, Van der Meer and De Waal (1990) found that oblique incidence tended to reduce the largest run-up heights more than the smaller run-up heights. This would indicate that the run-up is also Weibull-distributed ($b > 2$) for obliquely incident waves.

Here, the ratio $d_{toe}/H_{s,toe}$ was larger than 2.5, indicating that the run-up would be Rayleigh-distributed ($b = 2$). However, the waves were also very obliquely incident, indicating that the run-up might be Weibull-distributed ($b > 2$). The right panel of Figure 10 shows quite similar trends for both storm peaks, where the lower part (smaller run-up heights) shows a different inclination, but the upper part is almost straight. As the focus is mainly on the larger run-up heights, the following only considers the upper part of the graph. Since the upper part is almost straight, the wave run-up heights can be considered Weibull-distributed. Determining the tangent to the curves gives the shape factor b. The scale factor a can be determined by locating the value on the horizontal axis, which corresponds to an exceedance probability of $1 - 0.632 = 0.368$ on the vertical axis. Here, shape factors $b = 2.2$ (laser scanner 1) and $b = 2.4$ (laser scanner 2) were found for the first storm peak, whereas $b = 2.1$ was found for both laser scanners for storm peak 2. The value of the scale factor a was approximately 1.1 m for both storm peaks. The run-up thus follows a Weibull distribution that is quite close to

a Rayleigh distribution. These shape factors mean that the larger run-up heights were somewhat smaller than if they were Rayleigh-distributed. This indicates a credible limited influence of the obliquely incident waves on the value of b.

5.2 Wave run-up depths

The run-up depths as measured by the laser scanners were validated in Oosterlo et al. (2019, 2021), generally showing good results higher on the slope. At those locations, little spray and foam occurred. Larger deviations were found closer to the still water level, where the laser scanners overestimated the run-up depths due to the large amounts of foam and spray which were present there.

For the current measurements, no run-up depth data from other instruments are available. However, Van der Meer (2011) gives the linear relation $d_{2\%} = c_{d2\%}(R_{u2\%}$ - $z)$, which was based on Schüttrumpf (2001); Van Gent (2002). This relation was later included in EurOtop (2018), with $d_{2\%}$ [m] the run-up depth exceeded by 2% of the waves, $c_{d2\%}$ [-] a coefficient depending on the dike slope (see e.g. Van der Meer, 2011), $R_{u2\%}$ [m] the 2% run-up height, and z [m] an arbitrary height on the slope relative to the still water level. Note that these $d_{2\%}$ values are not the run-up depths corresponding to the $R_{u2\%}$ wave, but the 2%-exceedance values of the run-up depth at a certain location on the slope. In other words, the run-up depth at a certain location that is exceeded by 2% of the waves. These values at different locations along the slope may thus also correspond to different waves, as they are based on the statistics of the run-up depths at that specific location on the slope.

No consensus has been reached on the value of the coefficient $c_{d2\%}$ yet. Van der Meer (2011) compared the results of different small and large-scale lab tests where run-up depths were measured. Note that these depths were often measured at the transition between slope and crest, where the wave changes from up-rushing to horizontal. Van der Meer (2011) recommends $c_{d2\%} = 0.20$ for slopes of 1:3 and 1:4, $c_{d2\%} = 0.30$ for a slope of 1:6 and interpolation for slope angles in between these values. The present mean slope of 1:4.5 would then give $c_{d2\%} = 0.23$. However, the research on which Van der Meer (2011) based this recommendation, often found largely differing $c_{d2\%}$ values. All but one small-scale source give $c_{d2\%} = 0.20$-0.22, all for 1:3 and 1:4 slopes except Schüttrumpf (2001) with a 1:6 slope. On the other side, FlowDike 2 (Lorke et al., 2011) gave $c_{d2\%} = 0.29$, for a 1:6 slope. The only large-scale tests that were considered in Van der Meer (2011), those of Schüttrumpf (2001), were also performed on a 1:6 slope. There, $c_{d2\%} = 0.33$-0.34 was found. Hence, these discrepancies in $c_{d2\%}$ could either be due to the different slope angles or due to the differences between small and large-scale tests.

Therefore, the left panel of Figure 11 shows the relations for both $c_{d2\%} = 0.23$ (recommendation of Van der Meer (2011)) and $c_{d2\%} = 0.34$ (1:6 slope large-scale tests of Schüttrumpf (2001)), comparing them with the laser scanner results. Similar trends as found in Oosterlo et al. (2019, 2021) were found here, with the relation of Van der Meer (2011) giving somewhat larger values than the laser scanners at locations higher on the slope. Since the values in Figure 11 were based on the statistics at a certain location, different values were found for both laser scanners. This was caused by the very oblique incidence. However, overall the results of both laser scanners agree well. Better agreement was found with $c_{d2\%} = 0.23$ than with $c_{d2\%} = 0.34$. The legend of the left panel of Figure 11 gives the HH and NBI values for $c_{d2\%} = 0.23$. The data of storm peak 1 agree better than the data of storm peak 2, which lie somewhat below the $c_{d2\%} = 0.23$ line. As was explained in sub-section 5.1, the data quality of the second storm peak was lower.

The better agreement with $c_{d2\%} = 0.23$ might suggest that the discrepancies found in the literature were caused by the different slope angles, not by the differences between small and large-scale tests. From the video recordings of the present measurements, it was observed that sometimes spray occurred around the still water level, due to breaking waves. This was especially found for the larger waves. Furthermore, some foam and quite some entrained air were present. The right panel of Figure 11 gives a snapshot of a large up-rushing wave. The spray could potentially have influenced the results at $z = 0.20$ m, for which quite large run-up depths were found. Since the laser beam reflects off the spray and foam, the laser scanners measure run-up depths that include the spray, foam and entrained air. Another potential influence is the laser footprint and resolution. Lower on the slope, the laser footprint is larger and the laser resolution is lower, potentially giving less accurate results lower on the slope. However, the overall results can be deemed reliable.

The reasonable agreement between $c_{d2\%} = 0.23$ and the present data further seems to suggest that the influence of the wave angle of incidence on the run-up depths is small, as the previous research was performed with normally incident waves.

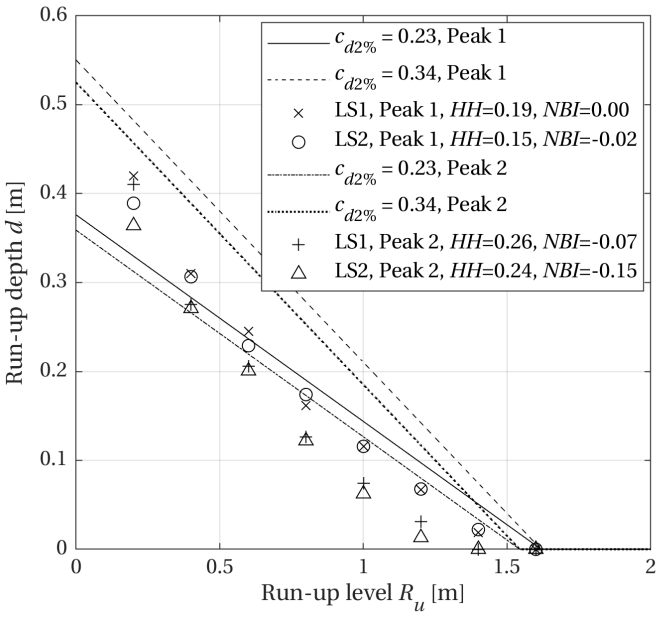

(a) Run-up depth.

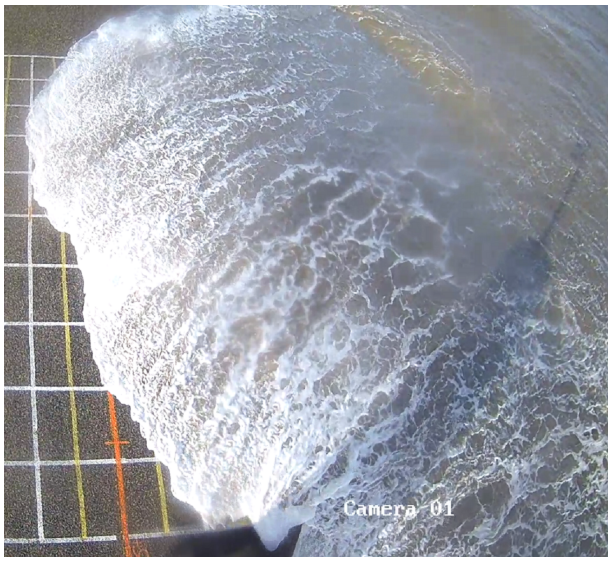

(b) Up-rushing wave.

Figure 11: Left: Run-up depth at several locations along the dike slope exceeded by 2% of the waves, based on both laser scanners and for both storm peaks. Data compared to linear relation of Van der Meer (2011) for two different values of $c_{d2\%}$. HH and NBI indicator values given for $c_{d2\%} = 0.23$. Right: Snapshot of large up-rushing wave, showing foam and entrained air.

5.3 Front velocities

Oosterlo et al. (2019, 2021) measured front velocities of normally incident waves with the laser scanners, and the time lag between the laser signals for obliquely incident waves (see Figure 8), and achieved good results. During storm Ciara the waves were very oblique, so these waves had a velocity component along the dike as well. Due to the very oblique incidence and breaking waves, defining a front is very difficult as is determining the 2D front velocities. Furthermore, during the present measurements, it was observed that even if a front was visible initially (lower on the dike slope), this front was then sometimes surpassed by another part of the oblique wave higher on the slope, effectively making that part the new 'front'.

The laser scanners only scan along two transects. The first one lies approximately 7 m from the far edge of the painted measurement grid, the second one lies approximately 9 m from the edge of the grid. Due to the oblique attack, the up-rushing waves travelled across the whole painted measurement grid, also see the right panel of Figure 11. Hence, the two laser transects missed quite a large part of the very oblique front running up the slope.

For the laser scanners, front velocities were determined by determining the velocity components along the a-axis (up the slope, along the laser lines, see Figure 7) first. These were combined with the delay between the laser signals (cross-correlation, velocity along the slope) to determine a 2D velocity. However, this did not yield good results, as the velocities along the slope were generally determined as being very large (small delay between the laser signals). Potentially, the offshore, but close to along-slope-directed wind played a role here as well. Thus, for the very obliquely incident waves present during storm Ciara, it was not possible to determine the actual 2D front velocities from the laser data accurately.

Therefore, only the highest ten run-ups for each storm peak were considered. Instead of 2D velocities, only the components travelling up the dike slope (along the a-axis) were considered. Results of both laser scanners were averaged and the maxima during each wave were determined. Even though it was not possible to estimate the 2D front velocities based on the laser scanner data, it was possible based on the video recordings. Figure 12 compares the 2D front velocities based on the videos and 1D front velocities based on the laser scanners for the

ten highest run-ups of each storm peak to the relation:

$$\frac{v_{front}}{\sqrt{gH_{m0}}} = c_u \sqrt{\frac{R_{u,max}}{H_{m0}}} \tag{8}$$

Equation 8 was taken from EurOtop (2018), where v_{front} [m/s] is the maximum front velocity for an individual wave and c_u [-] is a normally-distributed stochastic parameter with $\mu(c_u) = 1.0$ and $\sigma(c_u) = 0.25$. The figure also includes the FlowDike data (Lorke et al., 2011), to show the scatter.

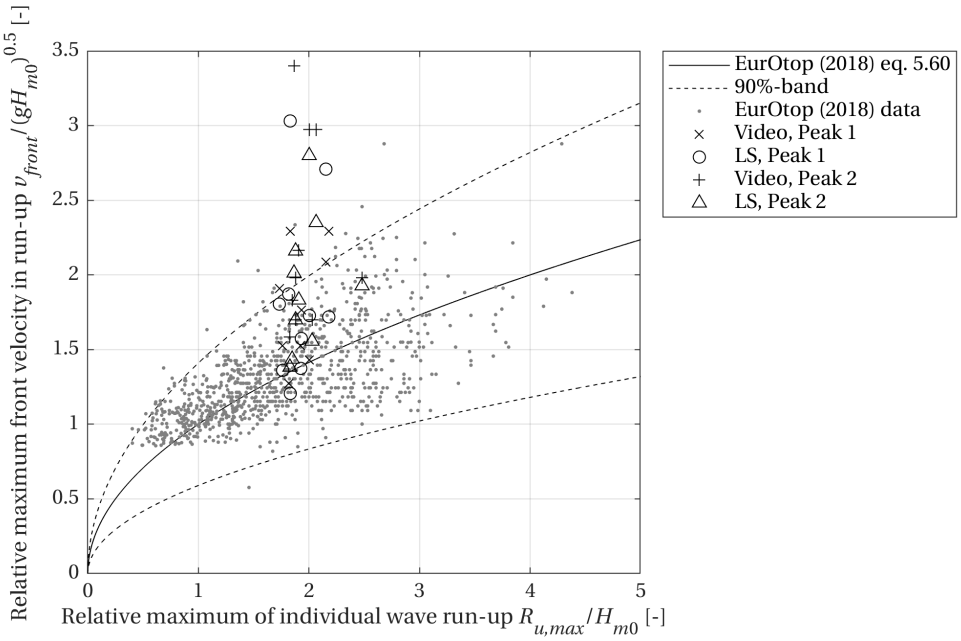

Figure 12: Relative maximum front velocity versus relative run-up on the slope. Results based on video analysis (2D velocities) and laser scanners (velocity component in the up-slope direction), compared to Equation 8. Figure based on EurOtop (2018), including the FlowDike data (Lorke et al., 2011).

Even these ten largest waves of both storm peaks propagated differently on the dike slope. Some waves had an initial direction mostly up the slope, later turning and becoming more alongslope-directed. Others were already very oblique from the beginning and travelled mostly along the slope. This again shows that Ciara posed very complicated conditions.

The video results are more reliable than the laser scanner results, since they represent actual 2D velocities. The front velocities as found here are generally larger than the relation that was based on the FlowDike small-scale tests with normally incident waves. One potential explanation for the differences is inaccuracy in determining the front velocities, either for the present measurements or for the FlowDike data. Some other potential explanations could be differences between small-scale tests and actual storms in the field, and differences between normally and obliquely incident waves. It is recommended to determine if improved front velocity results can be achieved with the laser system for future storms with less obliquely incident (but still oblique) waves.

5.4 Wave overtopping volumes and discharges

The (virtual) wave overtopping volumes and mean discharges were calculated using the same method as in Oosterlo et al. (2019, 2021), by integrating the run-up depths above a virtual crest level, and taking the maximum value of that volume within a wave period as the overtopping volume for that wave. Several virtual crest levels were considered, where one corresponds to the overtopping tank level (4.4 m+NAP). Figure 13 compares the results with the overtopping tank data, the EurOtop (2018) wave overtopping equations and the EurOtop (2018) data, which give an indication of the spread in the data. Table 2 gives the overtopping discharges, volumes and number of overtopping waves. With angles of incidence of 66° and 67°, the γ_β for the overtopping is 0.78.

Table 2: Run-up and overtopping parameters for both laser scanners, the video recordings, the overtopping tank and EurOtop (2018) equations at 4.4 m+NAP, for both storm peaks. V_{max} [l/m] is the maximum overtopping volume. Note that the table gives two values for several parameters. The two q values for EurOtop (2018) correspond to discharges based on the measured $T_{m-1,0}$ and based on the ratio $T_{m-1,0} = T_p/1.1$. The maximum volumes of EurOtop (2018) correspond to volumes calculated with Equation 10 - Equation 12, based on the EurOtop (2018) q, a and b values, or based on the laser scanner q, a and b values. The number of overtopping waves according to the video analysis correspond to the number of overtopping waves at the locations of laser lines 1 and 2.

	$R_{u2\%}$ [m]	q [l/s/m]	V_{max} [l/m]	N_{ow} [-]
Storm peak 1				
Laser scanner 1	1.62	0.118	100.0	43
Laser scanner 2	1.62	0.109	98.8	52
Video analysis	-	-	-	51 / 48
Overtopping tank	-	0.130	86.1	57
EurOtop (2018)	2.06	1.369 / 0.198	500.5 / 45.3	-
Storm peak 2				
Laser scanner 1	1.47	0.056	106.4	38
Laser scanner 2	1.50	0.067	121.5	39
Video analysis	-	-	-	47 / 50
Overtopping tank	-	0.107	71.2	55
EurOtop (2018)	1.86	0.952 / 0.102	501.5 / 43.8	-

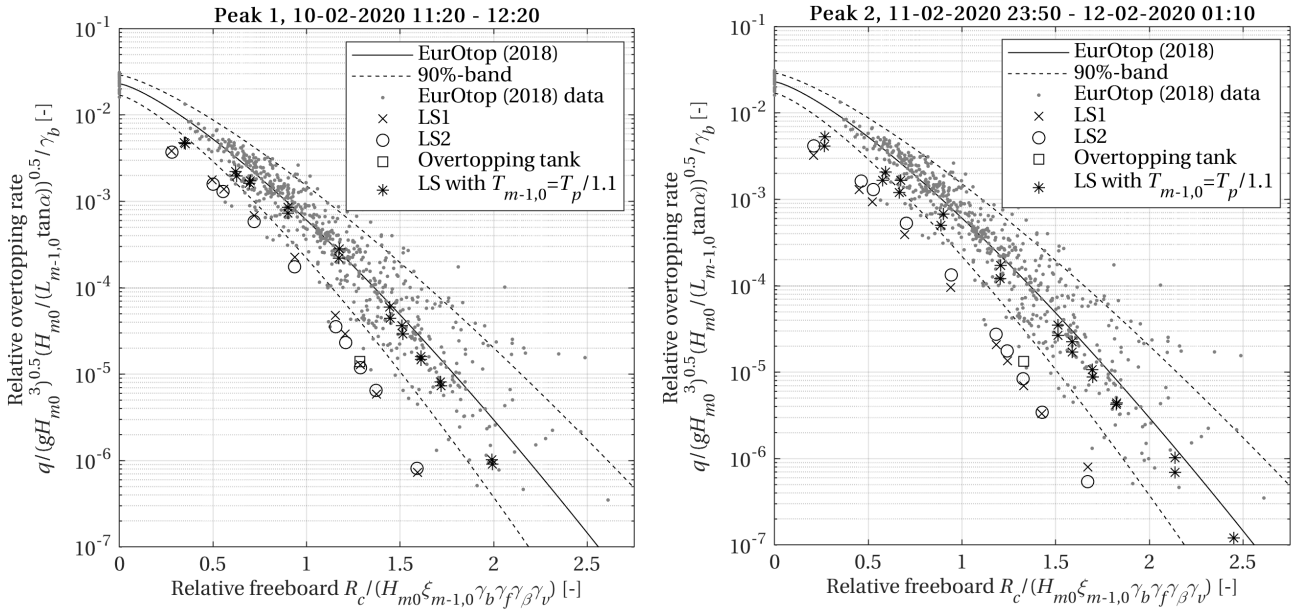

(a) Storm peak 1.

(b) Storm peak 2.

Figure 13: Relative overtopping rate for several virtual crest levels, based on both laser scanners (crosses, circles) and the overtopping tank (squares), for both storm peaks. The laser scanner data have also been plotted using the relation $T_{m-1,0} = T_p/1.1$ (asterisks). Results compared to EurOtop (2018) equations (solid and dashed lines) and data (dots). Figure based on EurOtop (2018). R_c [m] is the crest freeboard, $\xi_{m-1,0}$ [-] is the breaker parameter, the different γ parameters [-] are influence factors, see EurOtop (2018).

The trend of the laser data in Figure 13 agrees quite well with the EurOtop (2018) equations, but both the tank and the laser scanners gave smaller discharges than the equations. EurOtop (2018) predicts a 10 times larger discharge for both storm peaks than measured by the laser scanners and tank, also see Table 2. Here, a ratio $T_p/T_{m-1,0} = 0.9$ occurred (as measured by the radar attached to the Rijkswaterstaat pole, see Table 1), while a more common ratio for a JONSWAP spectrum is $T_p/T_{m-1,0} = 1.1$. Therefore, the laser data were also plotted using $T_{m-1,0} = T_p/1.1$ in Figure 13. Using this ratio, the lasers, tank and EurOtop (2018) agree much better. See also Table 2, where the EurOtop (2018) overtopping volumes and discharges using $T_{m-1,0} = T_p/1.1$ have also been given. Hence, the large deviations in the overtopping discharges mainly seem to stem from the $T_{m-1,0}$ wave period. Large $T_{m-1,0}$ values consistently occur during storms in the area of interest, indicating that low-frequency energy plays a role. The influence of low-frequency energy (and thus $T_{m-1,0}$ wave period) on the overtopping discharge predicted by the EurOtop (2018) equations is generally large (e.g. Lashley et al., 2020; Oosterlo et al., 2018). However, the low-frequency energy present during storm Ciara apparently did not influence the wave overtopping, as indicated by the much smaller measured wave overtopping discharges than predicted by EurOtop (2018) (with the measured $T_{m-1,0}$). This is contrary to expectations and the EurOtop (2018) equations, since Van Gent (1999*a*,*b*, 2001) found that the spectral shape does not affect the wave run-up and overtopping, as long as the $T_{m-1,0}$ is the same. If the measured $T_{m-1,0}$ is correct, this would indicate that the EurOtop (2018) equations may not be fit for use with the complex multi-modal spectra as often present in the Eems-Dollard estuary. Therefore, further research into the measured low-frequency energy and $T_{m-1,0}$ wave period, and into the influence of low-frequency energy on wave overtopping, is recommended.

The discharges as measured by the laser scanners and tank agree well, especially for the first storm peak. The tank gave a 1.5 - 2 times larger discharge than the laser scanners for the second peak. This can be explained using the right panel of Figure 9. Due to the somewhat lower data quality, the laser scanners gave a slight negative bias for the run-up heights of the second storm peak. Due to this underestimation of the run-up heights, some of the smaller overtopping waves, which just reached the overtopping tank, were missed, resulting in a somewhat smaller discharge than with the tank.

The percent exceedance distribution of overtopping wave volumes is given by a Weibull distribution (Hughes et al., 2012):

$$P_{v\%}\left(V_i \geq V\right) = exp\left[-\left(\frac{V}{a}\right)^b\right] \bullet (100\%) \tag{9}$$

where $P_{v\%}$ [%] is the percentage of wave volumes that will exceed the specified volume V_{i} [m^3/m]. b is the shape factor and a is the scale factor. The left panel of Figure 14 shows the fit for b according to Zanuttigh et al. (2014). A value for b of 0.75 has long been used to describe overtopping of individual wave volumes, but the graph shows that with larger relative discharge the b-value may increase significantly, leading to a gentler distribution of overtopping wave volumes (EurOtop, 2018). b-values were also calculated for the present measurements at several (virtual) crest levels, based on both the laser scanners and the overtopping tank. The laser scanner data follow the trend of the line quite well, but the b-values themselves are smaller. The exact cause of these smaller b-values is unknown. These smaller b-values mean that the distribution of overtopping wave volumes is steeper, meaning that the largest volumes are relatively larger. The overtopping tank data do agree well with the fit.

Table 2 also gives the maximum overtopping volumes V_{max} [l/m] for the laser scanners, overtopping tank and EurOtop (2018) equations for both storm peaks. The maximum overtopping volume can be calculated as follows, according to EurOtop (2018):

$$P_{ov} = \frac{N_{ow}}{N_w} \tag{10}$$

$$a = \left(\frac{1}{\Gamma\left(1+\frac{1}{b}\right)}\right)\left(\frac{qT_m}{P_{ov}}\right) \tag{11}$$

$$V_{max} = a\left[\ln\left(N_{ow}\right)\right]^{1/b} \tag{12}$$

with N_w [-] the number of incident waves, Γ the mathematical gamma function, P_{ov} [-] the probability of overtopping, T_m [s] the mean wave period and a the scale factor of the Weibull overtopping wave volumes

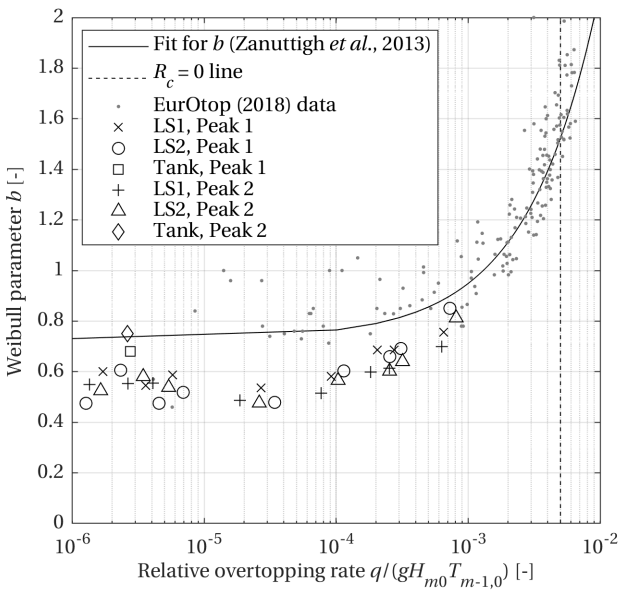

(a) Weibull shape factor b.

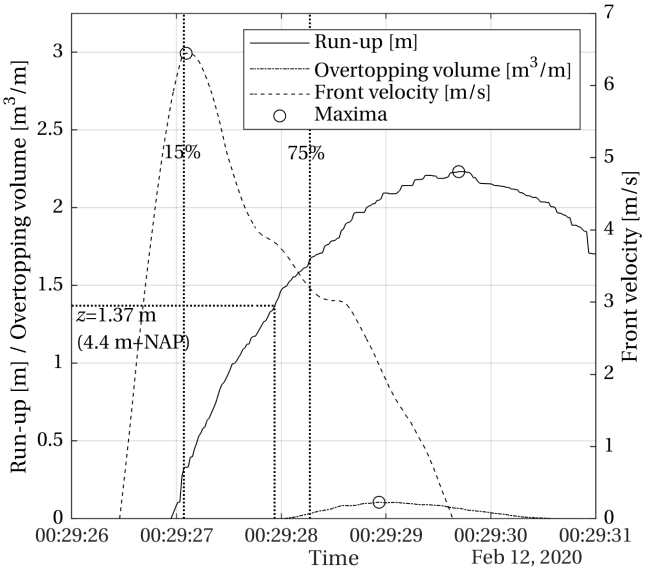

(b) Development of run-up, overtopping volume and front velocity over time.

Figure 14: Left: Weibull shape factor b for smooth structures and spanning a range of relative freeboards. Laser and overtopping tank data plotted for both storm peaks. Fit for b from Zanuttigh et al. (2014) shown as well. Figure based on EurOtop (2018). Right: Development of run-up, overtopping volume and front velocity over time for one large wave and based on data of one of the laser scanners. The dotted lines indicate the moments that the run-up reaches 15% and 75% of the maximum run-up level, and the moment that the run-up reaches the overtopping tank level.

distribution. These maximum volumes generally show more scatter, since they correspond to the maximum of a distribution.

The numbers of overtopping waves agree quite well for all instruments for storm peak 1, see Table 2. The laser scanners give fewer overtopping waves for the second storm peak. As explained above, this was caused by the underestimation of the run-up heights by the laser scanners for storm peak 2, leading to fewer run-up heights above the height level of the overtopping tank and thus fewer overtopping waves.

The maximum volumes of both laser scanners and the overtopping tank agree quite well for the first storm peak (15% larger volume with the laser scanners). The results differ more for the second storm peak, where the laser scanners gave a 50% to 70% larger maximum volume than the tank. As was explained above, the laser scanners measure the spray, foam and entrained air, which the overtopping tank does not. No spray was present above the height of the overtopping tank (4.4 m+NAP). However, some foam was present and entrained air was visible at the wave fronts. The volumes as measured with the laser scanners thus include this foam and air, and this can explain the larger maximum volumes as measured by the laser scanners. Since the data quality of the second storm peak was somewhat lower, the maximum volume during the second storm peak might have been slightly overestimated. This was potentially caused by the larger layer thickness threshold that had to be used. However, the influence of the larger threshold is at most a few l/m for the largest overtopping volume and even less for the smaller volumes. Not much is known about the actual air content in up-rushing waves. If the assumption is made that the differences between the maximum volumes were fully caused by the foam and entrained air, then that would mean that approximately 15% of the volume consists of foam and air. This amount seems reasonable when compared to visual observations of the up-rushing waves.

Another explanation that could be proposed is that the laser scanners provide 2D values of the overtopping, along the assumed infinitely thin laser line, whereas the overtopping tank gives overtopping volumes over a width of 4 m. With a large enough number of waves, this influence will average out, and it is therefore expected that this influence was small here.

The EurOtop (2018) equations give 4 to 6 times larger maximum volumes than the lasers and overtopping tank, when using the overtopping discharge q and the a and b-values (scale and shape factors) of the Weibull distribution according to EurOtop (2018) to determine these maximum volumes. The results agree much better,

if the q, a and b-values as found with the laser scanners are used instead to determine the maximum volume with Equation 10 - Equation 12. In that case, the EurOtop (2018) equations give maximum volumes that are 40% - 50% smaller than the volumes found by the laser scanners. Note that the $T_{m-1,0}$ is of influence here as well, as it is included in the EurOtop (2018) equations for both q and b.

The right panel of Figure 14 shows the development over time of the run-up height, overtopping volume and up-slope front velocity of one wave based on data of one of the laser scanners. The dotted lines indicate the moments that the run-up reaches 15% and 75% of the maximum run-up level, and the moment that the run-up reaches the overtopping tank level (4.4 m+NAP). For all measured waves that would have caused overtopping, the maximum front velocities were found between 15% to 75% of the maximum run-up height of that specific wave. This is in agreement with Van der Meer (2011). The largest volumes above the virtual crest were generally found just before or at the moment of maximum run-up height.

5.5 Wave periods and angles of incidence

As described in section 4, the wave peak periods and angles of incidence were determined with the method as described in Oosterlo et al. (2021). Hence, the wave peak periods were determined from the auto-spectral densities of the run-up signals. The angles of incidence were determined using the cross-spectral density of the run-up signals of both laser scanners, from which the time lag between both laser signals can be determined. The distance between the laser scan lines was then divided by the time lags, to determine the phase velocity of a projected wave travelling past the laser scanners. Using trigonometry and the incident wave celerity based on linear wave theory, the angle of incidence spectrum can be determined, see Figure 15. For the full description, refer to Oosterlo et al. (2021).

Figure 15 compares the variance density spectra based on the run-up signals $R_u(t)$ during both storm peaks, with variance density spectra as measured by the radar on the Rijkswaterstaat measurement pole (see the left panel of Figure 2 and Table 1). Note that the spectra based on the run-up signals do not represent a real wave spectrum, from which e.g. a wave height can be determined. The laser-based spectra also show much more variance content than the radar spectra, which are real wave spectra. The main observation is that much low-frequency energy is present in the run-up spectra. Although low-frequency energy is also present in the wave spectra, the low-frequency energy is not as prominent. The exact cause of this apparent large low-frequency energy is unknown, but may have been caused by some type of locally-generated surf-beat. The peak (wind) wave period T_p for storm peak 1 was determined as being 4.5 s, for the second storm peak this was 4.2 s. These values are quite close to the values of 4.35 s and 4.00 s that were derived from the radar measurements near the toe of the dike, see Table 1. Hence, quite a good estimate of the incident peak wave period can be obtained from the run-up signals.

The angle of incidence spectra give the angle of incidence β [°] relative to the dike normal for each mode in the spectra of the measured run-up, and are also given in Figure 15. They give a peak angle of incidence of 37° for storm peak 1 and 45° for storm peak 2. These angles of incidence are smaller than the angles of incidence as estimated at the dike toe of 66° and 67°, refer to Table 1. Hence, these results do not agree well, even though Oosterlo et al. (2021) achieved good results for angles of incidence up to 45°. A potential explanation for the differences could be that the up-rushing waves turned slightly more towards the dike normal on the shallow flat directly in front of the dike and on the dike slope. Furthermore, there exists some uncertainty in the mean wave direction and thus in the angle of incidence, since they were based on a relation between the wind direction and wave direction (Equation 1). However, the differences found here are rather large. This again highlights the complexities of storm Ciara and very obliquely incident waves. Further research is therefore recommended during storms with less oblique (but still oblique) wave attack.

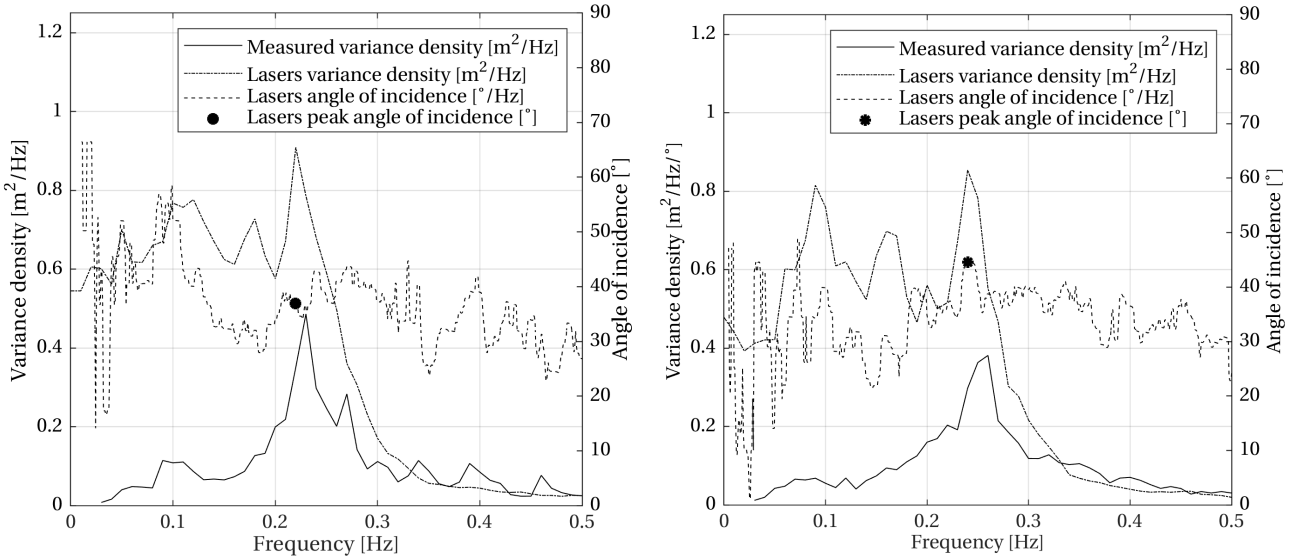

(a) Storm peak 1.

(b) Storm peak 2.

Figure 15: Wave variance density spectra based on radar measurements (solid lines), variance density spectra based on laser scanner run-up signals (dash-dot lines) and 'angle of incidence spectra' (dashed lines) for both storm peaks, giving the angle of incidence for each mode in the spectrum. The dots indicate the peak angles of incidence.

6 Conclusions

This paper presents the first field measurements with an innovative laser scanner system during an actual severe winter storm with very oblique wave attack. The system can measure wave run-up heights, depths and front velocities. From the measured data the wave overtopping, (peak) wave period and angle of incidence can also be calculated. The paper describes the analysis of the data obtained during storm Ciara (10 - 12 February 2020) and validates the results with data from overtopping tanks and video recordings.

Ciara was a highly unique and complex storm, with offshore-directed wind at the measurement location and waves that refracted somewhat on the shallow flats in front of the dike to become almost alongshore-directed waves at the dike. This posed large challenges for measuring the 2D front velocities.

The run-up heights based on measured distances agreed well with the run-up observed in video recordings. Run-up heights based on laser reflectance did not agree well, caused by interference of the grid painted on the slope for the video analysis. By removing several of the grid lines good results are expected to be achieved during future storms. The water depth was relatively deep, the waves were breaking and the run-up was very oblique during Ciara. The oblique wave run-up during Ciara was Weibull-distributed (b = 2.1-2.4), quite close to a Rayleigh distribution but with somewhat smaller largest run-up heights.

Reasonable agreement between the measured run-up depths and the relation of Van der Meer (2011) with $c_{d2\%} = 0.23$ was found. Discrepancies in the $c_{d2\%}$-values as found in the literature seem to be caused by the different dike slope angles that were used, rather than caused by differences between small and large-scale tests. The results further seem to suggest that the influence of the wave angle of incidence on the run-up depths is small. However, further research is recommended.

Previous research achieved good results for measuring front velocities of normally incident waves with the laser scanners. Due to the very oblique incidence during storm Ciara, it was very difficult to define a front of the waves, which often ran up the slope in a sort of sideways and local plunging motion, with a larger along-slope-directed velocity higher on the slope. To determine the 2D front velocities based on just the two laser scanner transects was even more complex. It was possible to estimate the 2D front velocities based on the video recordings. The velocities as found here were larger than the relation of EurOtop (2018), which was based on small-scale, normally incident waves. The most likely causes for the differences are inaccuracies in determining the front velocities, differences between small-scale tests and actual storms in the field, and differences between normally and obliquely incident waves.

Overtopping discharges of both the lasers and overtopping tank agreed well. Trends of the calculated overtopping discharges agreed reasonably well with the EurOtop (2018) equations, but the values themselves were smaller than according to the equations. This mainly arose from the $T_{m-1,0}$ wave period, which was relatively large here ($T_p/T_{m-1,0} = 0.9$), indicating that low-frequency energy was present during storm Ciara. Applying $T_p/T_{m-1,0} = 1.1$ of a typical JONSWAP spectrum, resulted in much better agreement between lasers, tank and EurOtop (2018) equations. This would indicate that the low-frequency energy present during storm Ciara did not influence the wave overtopping. This is contrary to expectations and the EurOtop (2018) equations, since Van Gent (1999*a*,*b*, 2001) found that the spectral shape does not affect the wave run-up and overtopping. If the measured $T_{m-1,0}$ is correct, this would indicate that the EurOtop (2018) equations may not be fit for use with the complex multi-modal spectra as often present in the Eems-Dollard estuary. Therefore, it is recommended to study the presence of low-frequency energy and the $T_{m-1,0}$ measurements in the area in more detail, and the influence of low-frequency energy on wave overtopping.

b-values of the Weibull distribution of overtopping wave volumes of the laser scanners were smaller than the fit of Zanuttigh et al. (2014), but the trend of the data agreed well. *b*-values based on the overtopping tank data agreed well with the fit. Maximum overtopping volumes of lasers and tank agreed reasonably well. EurOtop (2018) gave larger maximum volumes based on the q, a and b predicted by EurOtop (2018), but smaller volumes based on the q, a and b of the laser scanners.

The peak wave period could be determined accurately from the run-up time signals. The angle of incidence of the incoming wave field, based on the laser data, was less oblique than that estimated using an analytical relation, even though good results were achieved using the same method (Oosterlo et al., 2021). Once again, the very oblique, almost coast-parallel, wave attack during Ciara posed large challenges. For further verification of the system, it is recommended to measure in the field at real dikes and during real storms with less oblique (but still oblique) wave attack.

The mobile system will be used at several different locations in the measurement campaign in the area over the coming years. The laser scanners can be installed on any dike; the performance of the system was confirmed for both asphalt and grass dike slopes. Some of the generic results, obtained from the measurements during storm Ciara, are that the wave run-up heights of very obliquely incident breaking waves in relatively deep water are Weibull-distributed, and that the run-up depth equation (Van der Meer, 2011) based on lab measurements also predicts the depths for an actual storm with oblique wave attack quite well. Furthermore, the trend of the EurOtop (2018) equations agrees quite well with measurements of very oblique wave overtopping, but measured discharges were smaller than according to the equations. Accurate measurements of the $T_{m-1,0}$ wave period and angle of incidence are important for further verification of the EurOtop (2018) equations and laser scanner system, and further measurements with the system during storms are expected to provide more insight into both the performance of the system and the understanding of oblique wave run-up and overtopping.

Acknowledgements

This study was made possible by the inspiring input of the late Gerbrant van Vledder. We would like to thank Gerben van der Meer, Jan Bakker and Frans Roorda for their help with setting up the laser scanner system, as well as Rik Wegman for his help in analysing the video recordings. This study was supported by Waterschap Noorderzijlvest and the Hoogwaterbeschermingsprogramma.

Author contributions (CRediT)

PO: conceptualisation, methodology, software, validation, formal analysis, investigation, data curation, writing – original draft, writing – review & editing, visualisation, project administration. BH: conceptualisation, methodology, software, validation, writing – review & editing, visualisation, supervision. JvdM: conceptualisation, methodology, validation, investigation, resources, writing – review & editing, supervision, project administration, funding acquisition. MO: methodology, software, formal analysis, investigation, resources, writing – review & editing. GJS: methodology, investigation, resources, writing – review & editing, supervision, project administration, funding acquisition.

Notations

Name	Symbol	Unit
Dimensional scale factor of Weibull distribution	a	
Non-dimensional shape factor of Weibull distribution	b	-
Van der Meer (2011) coefficient in run-up depth equation, dependent on the dike slope	c_d	-
EurOtop (2018) coefficient in run-up front velocity equation	c_u	-
Water depth, run-up depth	d	m
Frequency	f	Hz
Water level	h	m
Significant wave height, based on mean of highest one-third of waves in a record	$H_{1/3}$	m
Significant wave height, based on spectral analysis	H_{m0}	m
Height of laser scanner above dike slope	h_s	m
Model data	M	
Number of waves in record, number of observations, Fourier transform window length	N	-
Number of overtopping waves	N_{ow}	-
Number of incident waves	N_w	-
Observation data	O	
Probability of overtopping	P_{ov}	-
Percentage of wave volumes that exceed a specified volume V_i	$P_{v\%}$	%
Mean wave overtopping discharge	q	l/s/m
Distance measured by laser scanner	R	m
Run-up height	R_u	m
Run-up height, exceeded by 2% of the number of incoming waves	$R_{u2\%}$	m
Spectral density	S	m^2/Hz
Mean wave period	T_m	s
Significant wave period, based on mean of highest one-third of waves in a record	$T_{1/3}$	s
Spectral wave period, based on spectral moments m_{-1}/m_0, with $m_n = \int_0^{\inf} Sf^n\, df$	$T_{m-1,0}$	s
Wave peak period, based on spectral analysis	T_p	s
(Virtual) overtopping volume	V	l/m
Run-up front velocity	v_{front}	m/s
Maximum (virtual) overtopping volume during a certain period of time	V_{max}	l/m
Wind direction	W_{dir}	°N
Wind velocity	W_{vel}	m/s
x-coordinate of laser scanner	x_s	m
z-coordinate of laser scanner pole	z_p	m
Mathematical gamma function	Γ	
Wave angle of incidence, wave angle of incidence spectrum	β	°, °/Hz
(Mean) wave direction relative to north	δ	°N
EurOtop (2018) influence factor for angle of wave attack	γ_β	-
Mean value of normally distributed parameter	μ	
Slant angle of laser scanner	ϕ	°
Correction angle, rotating laser scanner coordinate system	ψ	°
Standard deviation of normally-distributed parameter	σ	
Scan angle of laser scanner	θ	°
Iribarren number/breaker parameter/surf similarity based on spectral wave steepness $s_{m-1,0}$	$\xi_{m-1,0}$	-
Global Positioning System	GPS	
Hanna and Heinold (1985) indicator	HH	
JOint North Sea WAve Project (Hasselmann et al., 1973)	JONSWAP	
Laser Imaging Detection And Ranging	LIDAR	
Not a Number	NaN	
Normaal Amsterdams Peil, Dutch ordnance level	NAP	
Normalised Bias Indicator	NBI	
Root-Mean-Square Error	RMSE	
Received Signal Strength Indicator	RSSI	

References

Battjes, J.A. and Groenendijk, H.W. (2000). Wave height distributions on shallow foreshores. *Coastal Engineering*, **40**(3), 161–182. ISSN 03783839. doi:10.1016/S0378-3839(00)00007-7.

Brodie, K.L., Slocum, R.K. and McNinch, J.E. (2012). New insights into the physical drivers of wave runup from a continuously operating terrestrial laser scanner. In: *2012 Oceans*, 1–8. IEEE. ISBN 978-1-4673-0829-8. doi:10.1109/OCEANS.2012.6404955.

Cete, C. (2019). *Quantifying the effect of woody vegetation on the wave loads on a dike using remote sensing. Large scale physical model tests.* Msc thesis, Delft University of Technology.

De Rouck, J., Verhaeghe, H. and Geeraerts, J. (2009). Crest level assessment of coastal structures — General overview. *Coastal Engineering*, **56**(2), 99–107. ISSN 03783839. doi:10.1016/j.coastaleng.2008.03.014.

De Vries, S., Hill, D., de Schipper, M. and Stive, M. (2011). Remote sensing of surf zone waves using stereo imaging. *Coastal Engineering*, **58**(3), 239–250. ISSN 03783839. doi:10.1016/j.coastaleng.2010.10.004.

EurOtop (2018). *Manual on wave overtopping of sea defences and related structures. An overtopping manual largely based on European research, but for worldwide application.* Second edition.

Hanna, S.R. and Heinold, D.W. (1985). *Development and application of a simple method for evaluating air quality models.* 4409. American Petroleum Institute, Washington, D.C.

Hasselmann, K., Barnett, T.P., Bouws, E., Carlson, H., Cartwright, D.E., Enke, K., Ewing, J.A., Gienapp, H., Hasselmann, D.E., Kruseman, P., Meerburg, A., Mueller, P., Olbers, D.J., Richter, K., Sell, W. and Walden, H. (1973). Measurements of wind-wave growth and swell decay during the Joint North Sea Wave Project (JONSWAP). *Deutches Hydrographisches Zeitschrift*, **8**(12), 1–95.

Hofland, B., Diamantidou, E., Van Steeg, P. and Meys, P. (2015). Wave runup and wave overtopping measurements using a laser scanner. *Coastal Engineering*, **106**, 20–29. ISSN 0378-3839. doi:10.1016/j.coastaleng.2015.09.003.

Hughes, S.A., Thornton, C.I., Van der Meer, J.W. and Scholl, B.N. (2012). Improvements in describing wave overtopping processes. In: *Coastal Engineering Proceedings*, volume 1, 35. ASCE, Santander, Spain. ISSN 2156-1028. doi:10.9753/icce.v33.waves.35.

Lashley, C.H., Bricker, J.D., Van der Meer, J.W., Altomare, C. and Suzuki, T. (2020). Relative Magnitude of Infragravity Waves at Coastal Dikes with Shallow Foreshores: A Prediction Tool. *Journal of Waterway, Port, Coastal, and Ocean Engineering*, **146**(5), 04020034. ISSN 0733-950X. doi:10.1061/(ASCE)WW.1943-5460.0000576.

Lorke, S., Brüning, A., Van der Meer, J.W., Schüttrumpf, H., Bornschein, A., Gilli, S., Pohl, R., Spano, M., Říha, J., Werk, S. and Schlütter, F. (2011). On the effect of current on wave run-up and wave overtopping. In: *Coastal Engineering Proceedings*, volume 1, 13. ASCE, Shanghai, China. ISSN 2156-1028. doi:10.9753/icce.v32.structures.13.

Matias, A., Blenkinsopp, C.E. and Masselink, G. (2014). Detailed investigation of overwash on a gravel barrier. *Marine Geology*, **350**, 27–38. ISSN 00253227. doi:10.1016/j.margeo.2014.01.009.

Mentaschi, L., Besio, G., Cassola, F. and Mazzino, A. (2013). Problems in RMSE-based wave model validations. *Ocean Modelling*, **72**, 53–58. ISSN 14635003. doi:10.1016/j.ocemod.2013.08.003.

Nielsen, P. and Hanslow, D.J. (1991). Wave runup distributions on natural beaches. *Journal of Coastal Research*, **7**(4), 1139–1152. ISSN 0749-0208.

Oosterlo, P., Hofland, B., Van der Meer, J.W., Overduin, M. and Steendam, G.J. (2021). Calibration and preparation of field measurements of oblique wave run-up and overtopping on dikes using laser scanners. *Coastal Engineering*, **167**(103915), 1–13. ISSN 03783839. doi:10.1016/j.coastaleng.2021.103915.

Oosterlo, P., Hofland, B., Van der Meer, J.W., Overduin, M., Steendam, G.J., Nieuwenhuis, J.W., Van Vledder, G.P., Steetzel, H. and Reneerkens, M. (2019). Measuring (Oblique) Wave Run-Up and Overtopping with Laser Scanners. In: *Proc. Coastal Structures*, 442–452. Bundesanstalt für Wasserbau, Hannover, Germany. doi:10.18451/978-3-939230-64-9_045.

Oosterlo, P., McCall, R., Vuik, V., Hofland, B., Van der Meer, J.W. and Jonkman, S. (2018). Probabilistic Assessment of Overtopping of Sea Dikes with Foreshores including Infragravity Waves and Morphological Changes: Westkapelle Case Study. *Journal of Marine Science and Engineering*, **6**(2), 48. ISSN 2077-1312. doi:10.3390/jmse6020048.

Pullen, T., Silva, E., Brown, J., Yelland, M., Pascal, R., Pinnell, R., Cardwell, C. and Jones, D. (2019). WireWall–laboratory and field measurements of wave overtopping. In: *Proc. Coastal Structures*, 1170–1179. Bundesanstalt für Wasserbau, Hannover, Germany. doi:10.18451/978-3-939230-64-9_117.

Schüttrumpf, H.F.R. (2001). *Wellenüberlaufströmung bei See-deichen. Experimentelle und theoretische Untersuchungen*. Dissertation, Technischen Universität Carolo-Wilhelmina zu Braunschweig. doi:10.24355/dbbs.084-200511080100-46.

Stam, C. (1989). Taluds van losgestorte materialen. Golfoploop op statisch stabiele stortsteen taluds onder golfaanval. Deel III, verslag modelonderzoek. Technical report m1983 deel iii, Waterloopkundig Laboratorium/WL, Delft, the Netherlands.

Streicher, M., Hofland, B. and Lindenbergh, R.C. (2013). Laser Ranging for Monitoring Water Waves in the New Deltares Delta Flume. In: *ISPRS Annals of the Photogrammetry, Remote Sensing and Spatial Information Sciences*, volume 2, 271–276. ISPRS, Antalya, Turkey. ISSN 21949050. doi:10.5194/isprsannals-II-5-W2-271-2013.

Van der Meer, J.W. (2011). The Wave Run-up Simulator. Idea, necessity, theoretical background and design. Technical report vdm11355, Van der Meer Consulting B.V., Heerenveen, the Netherlands.

Van der Meer, J.W. (2018). Meerjarige Veldmetingen Eems-Dollard. Te verwachten stormomstandigheden en bepalen hoogte van de golfoverslagbakken in de dijk bij Uithuizerwad. Technical report, Van der Meer Consulting B.V., Akkrum, the Netherlands.

Van der Meer, J.W. and Bruce, T. (2014). New Physical Insights and Design Formulas on Wave Overtopping at Sloping and Vertical Structures. *Journal of Waterway, Port, Coastal, and Ocean Engineering*, **140**(6), 04014025. ISSN 0733-950X. doi:10.1061/(ASCE)WW.1943-5460.0000221.

Van der Meer, J.W. and De Waal, J.P. (1990). Invloed van scheve inval en richtingspreiding op golfoploop en overslag. Verslag modelonderzoek. Technical report h638, Waterloopkundig Laboratorium/WL, Delft, the Netherlands.

Van der Meer, J.W. and De Waal, J.P. (1993). Waterbeweging op taluds. Invloed van berm, ruwheid, ondiep voorland en scheve lang- en kortkammige golfaanval. Technical report h1256-b, Waterloopkundig Laboratorium/WL, Delft, the Netherlands.

Van der Meer, J.W., Nieuwenhuis, J.W., Steendam, G.J., Reneerkens, M., Steetzel, H. and Van Vledder, G.P. (2019). Wave Overtopping Measurements at a Real Dike. In: *Proc. Coastal Structures*, 1107–1117. Bundesanstalt für Wasserbau, Hannover, Germany. doi:10.18451/978-3-939230-64-9_111.

Van Gent, M.R.A. (1999*a*). Physical model investigations on coastal structures with shallow foreshores: 2D model tests with single and double-peaked wave energy spectra. Technical report, WL — Delft Hydraulics, Delft, the Netherlands.

Van Gent, M.R.A. (1999*b*). Wave run-up and wave overtopping for double-peaked wave energy spectra. Technical report, WL — Delft Hydraulics, Delft, the Netherlands.

Van Gent, M.R.A. (2001). Wave Runup on Dikes with Shallow Foreshores. *Journal of Waterway, Port, Coastal, and Ocean Engineering*, **127**(5), 254–262. ISSN 0733-950X. doi:10.1061/(ASCE)0733-950X(2001)127:5(254).

Van Gent, M.R.A. (2002). Low-exceedance wave overtopping events: Measurements of velocities and the thickness of water-layers on the crest and inner slope of dikes. Technical report dc030202/h3803, WL — Delft Hydraulics, Delft.

Vousdoukas, M.I., Kirupakaramoorthy, T., Oumeraci, H., De la Torre, M., Wübbold, F., Wagner, B. and Schimmels, S. (2014). The role of combined laser scanning and video techniques in monitoring wave-by-wave swash zone processes. *Coastal Engineering*, **83**, 150–165. ISSN 03783839. doi:10.1016/j.coastaleng.2013.10.013.

Vousdoukas, M.I., Wziatek, D. and Almeida, L.P. (2012). Coastal vulnerability assessment based on video wave run-up observations at a mesotidal, steep-sloped beach. *Ocean Dynamics*, **62**(1), 123–137. ISSN 1616-7341. doi:10.1007/s10236-011-0480-x.

Wenneker, I., Spelt, B., Peters, H. and De Ronde, J. (2016). Overview of 20 years of field measurements in the coastal zone and at the Petten sea dike in the Netherlands. *Coastal Engineering*, **109**, 96–113. ISSN 03783839. doi:10.1016/j.coastaleng.2015.12.009.

Zanuttigh, B., Van der Meer, J.W., Bruce, T. and Hughes, S. (2014). Statistical characterisation of extreme overtopping wave volumes. In: *Coasts, Marine Structures and Breakwaters 2013*, 442–451. ICE Publishing, Edinburgh, Scotland. doi:10.1680/fsts.59757.048.